1 *Article*

2,3 GEO-GEO Stereo-Tracking of Atmospheric Motion Vectors (AMVs) from the Geostationary Ring

4 **James L. Carr [1,*] , Dong L. Wu [2] , Jaime Daniels [3] , Mariel D. Friberg [2,4] , Wayne Bresky [5] and**
5 **Houria Madani [1]**

6 [1] Carr Astronautics, 6404 Ivy Lane, Suite 333, Greenbelt, MD 20770, USA; jcarr@carrastro.com
7 [2] NASA Goddard Space Flight Center, Greenbelt, MD 20770, USA; dong.l.wu@nasa.gov
8 [3] NOAA/NESDIS Center for Satellite Applications and Research, College Park, MD 20740, USA
9 [4] Universities Space Research Association, Columbia, MD 21046, USA
10 [5] I.M. Systems Group (IMSG), Rockville, MD 20852, USA
11 * Correspondence: jcarr@carrastro.com

13 **Abstract:** Height assignment is an important problem for satellite measurements of Atmospheric
14 Motion Vectors (AMVs) that are interpreted as winds by forecast and assimilation systems.   Stereo
15 methods assign heights to AMVs from the parallax observed between observations from different
16 vantage points in orbit while tracking cloud or moisture features.   In this paper, we fully develop
17 the stereo method to jointly retrieve wind vectors with their geometric heights from geostationary
18 satellite pairs.   Synchronization of observations between observing systems is not required.
19 NASA and NOAA stereo-winds codes have implemented this method and we have processed large
20 datasets from GOES-16, -17, and Himawari-8.   Our retrievals are validated against rawinsonde
21 observations and demonstrate the potential to improve forecast skill.   Stereo winds also offer an
22 important mitigation for the loop heat pipe anomaly on GOES-17 during times when warm focal
23 plane temperatures cause infra-red channels that are needed for operational height assignments to
24 fail.   We also examine several application areas, including deep convection in tropical cyclones,
25 planetary boundary layer dynamics, and fire smoke plumes, where stereo methods provide insights
26 into atmospheric processes.   The stereo method is broadly applicable across the geostationary ring
27 where systems offering similar Image Navigation and Registration (INR) performance as GOES-R
28 are deployed.

29 **Keywords:** 3D-winds; atmospheric motion vectors (AMVs); GOES-R; ABI; Himawari; AHI;
30 planetary boundary layer (PBL); stereo imaging; parallax; Image Navigation and Registration (INR)

32 1. Introduction

33   Geostationary satellite wind products rely on the tracking of cloud or moisture features in multi-
34 temporal sequences of scenes from a single satellite.   This method provides a good means of
35 determining the Atmospheric Motion Vector (AMV) vector but does not directly observe the AMV
36 height within the atmosphere.   There are several indirect methods for making AMV height
37 assignments that rely on infra-red (IR) brightness temperatures regardless of whether the feature is
38 being tracked in an IR or a Visible (VIS) spectral channel.   Fundamentally these methods rely on a
39 radiative transfer model based on differential absorption by gas species from the cloud top into space
40 or the use of Numerical Weather Prediction (NWP) forecast temperature profiles. [1-8].
41 Complicated thermodynamics can cause problems for IR height assignments that are made based on
42 a modeled temperature profile.
43   We argue that stereo methods, which provide a direct observation of the AMV height through
44 geometric parallax, have advantages where there is overlapping coverage by two satellites.   The
45 same template that is tracked in time can be observed from two different platforms and its altitude
46 inferred from the observed parallax.   Such an approach directly ties the AMV to its height.   Stereo

47 imaging from two geostationary (GEO) satellites is an old idea [9] that has been given new life with
48 the new generation of GEO satellites such as the Geostationary Operational Environmental Satellites
49 R-series (GOES-R) operated by the U.S. National Oceanic and Atmospheric Administration (NOAA)
50 that offer imagery with much improved Image Navigation and Registration (INR), i.e., geometric
51 accuracy and stability. We discuss the sensitivity of stereo-wind retrievals to INR and other errors
52 in Section 4 of this paper.

53 This paper draws on our previously published work in stereo winds [10,11] combining Low-
54 Earth Orbiting (LEO) and GEO imagery and demonstrating stereo winds using the prior (GOES-NOP)
55 generation of GOES satellites. Our methods, explained in Section 2, do not require that the satellite
56 observations be synchronous with each other in time. Only pixel sampling times need to be known,
57 or accurately modeled, so that an AMV can be jointly solved with its stereo height. This relaxed
58 sampling requirement enables stereo winds to be produced from a heterogeneous constellation that
59 includes pairs in the GEO ring, or LEO-GEO pairs filling gaps in the overlaps between GEO satellites.
60 Other work [12,13] on stereo measurements of cloud-top heights (hence AMV height assignment)
61 assumes synchronous observations, but Merucci, et. al. [14] describes a method that adjusts for non-
62 simultaneous observations when using the parallax to measure the height of volcanic ash plumes.

63 Our results, in Section 3, include several applications where jointly determined AMVs and
64 stereo-wind heights provide new insights into some outstanding mesoscale atmospheric dynamic
65 problems: convection and tropical cyclones, Planetary Boundary Layer (PBL), and wildfire plumes.
66 Ultimately, we anticipate that operational stereo winds will benefit numerical weather modeling by
67 providing more, high quality AMVs with accurate height assignments. We demonstrate this
68 potential by validating our stereo winds against rawinsonde observations and comparing these to
69 NOAA's operational winds. These results reveal a clear benefit to stereo winds. While beneficial
70 in the general case, stereo winds are particularly quite useful for AMV height assignments in the
71 presence of the Loop-Heat Pipe (LHP) anomaly [15,16] when GOES-17 loses its ability to assign AMV
72 heights due to anomalously warm focal plane temperatures during certain times of day near the
73 equinoxes. In such cases, some IR bands remain operational for AMVs, but others used for IR height
74 assignment in the operational algorithms become nonfunctional. Stereo methods can mitigate the
75 impact of the LHP anomaly on operational winds from GOES-17 in the overlaps between GOES-17
76 and -16 and GOES-17 and Himawari-8. This is extensively discussed in Section 3.

2. Materials and Methods

78 This paper works with data from the American GOES-R satellites (GOES-16 and -17) and the
79 Japanese Himawari-8 spacecraft. The GOES-R spacecraft carries the Advanced Baseline Imager
80 (ABI) [17,18], which is a 16-channel imager generally covering the Full Disk (FD) of the Earth once
81 every 10 minutes from geostationary orbit, a region covering the Continental U.S. (CONUS) or Pacific
82 U.S. (PACUS) every 5 minutes, and two Mesocale (MESO) frames every 1 minute. The Himawari-8
83 spacecraft carries a similar instrument, the Advanced Himawari Imager (AHI) [19]. We only work
84 with the AHI FD frames to guarantee geographically overlapping coverage with ABI on GOES-17.
85 The AHI FDs also refresh every 10 minutes. Both ABI and AHI were manufactured by L3Harris in
86 Ft. Wayne, Indiana USA and are nearly identical in design and construction except for the differences
87 noted in Table 1. AHI offers true-color imaging with a green channel, not present with ABI, while
88 ABI has a near-infrared (NIR) channel (ABI Band 4), where water vapor is a strong absorber, that is
89 useful for the observation of cirrus clouds. There is one channel (Band 5) shared by both that has a
90 finer spatial resolution in ABI. All mid- and long-wave IR channels share very similar spectral and
91 spatial characteristics.

92 **Table 1.** ABI and AHI spectral channels match very closely except for a green channel (AHI Band 2)
93 that ABI lacks and a NIR water vapor absorption band (ABI Band 4) that AHI lacks. Their common
94 Bands 5 also have different resolutions.

GOES-R (ABI)					Himawari-8 (AHI)				
ABI	Resolution	Center	Bandwidth	Bit	AHI	Resolution	Center	Bandwidth	Bit

Band	(km)*	Wavelength (µm)	(µm)	Depth	Band	(km)	Wavelength (µm)	(µm)	Depth
1	1	0.47	0.04	10	1	1	0.4703	0.0407	11
					2	1	0.5105	0.0308	11
2	0.5	0.64	0.10	12	3	0.5	0.6399	0.0817	11
3	1	0.8655	0.039	10	4	1	0.8563	0.0345	11
4	2	1.3785	0.015	11					
5	1	1.61	0.06	10	5	2	1.6098	0.0409	11
6	2	2.250	0.050	10	6	2	2.257	0.0441	11
7	2	3.90	0.20	14	7	2	3.8848	0.2006	14
8	2	6.185	0.83	12	8	2	6.2383	0.8219	11
9	2	6.95	0.40	11	9	2	6.9395	0.4019	11
10	2	7.34	0.2	12	10	2	7.3471	0.1871	12
11	2	8.5	0.4	12	11	2	8.5905	0.3727	12
12	2	9.61	0.38	11	12	2	9.6347	0.3779	12
13	2	10.35	0.5	12	13	2	10.4029	0.4189	12
14	2	11.2	0.8	12	14	2	11.2432	0.6678	12
15	2	12.3	1.0	12	15	2	12.3828	0.9656	12
16	2	13.3	0.6	10	16	2	13.2844	0.5638	11

* "1km" for GOES-R is 28.0 µradians; for Himawari, it is exactly 1km at the Subsatellite Point (SSP).

The ABI and AHI Level-1 products are both constructed on a fixed grid by resampling calibrated detector samples to form pixels. Each fixed-grid pixel on the Earth has an invariant geographic location assigned to it. The Image Navigation and Registration (INR) process assures the accuracy and stability of the true positions of pixels with respect to their assigned fixed-grid locations. Both fixed grids define their pixel sites in integer and half-integer angular increments of nominal kilometers in accordance with the spatial resolution of the channel. The AHI fixed grid defines a nominal kilometer to be the angular measure of 1 km on the ground at the subsatellite point, which is slightly less than the nominal kilometer used by the ABI fixed grid of exactly 28 µrad. The AHI FD Level-1 product has 22000x22000 pixels at 0.5 km resolution, whereas the 0.5-km ABI FD product is 21696x21696 pixels. The mapping between fixed-grid angles and geographic coordinates is also different. This is defined for ABI in the GOES-R Product User's Guide (PUG) [20] and for AHI by the Normalized Geostationary Projection defined in a Coordination Group for Meteorological Satellites (CGMS) specification [21]. Both fixed grids are defined with respect to an idealized satellite placed on the equator at a reference longitude, with the geographic assignment for a pixel being the longitude and geodetic latitude where the line-of-sight from the idealized satellite pierces the reference ellipsoid – effectively the 1984 World Geodetic System (WGS 84).

2.1 GOES-GEO Stereo Winds Coverage

Figure 1 shows the coverage for stereo winds using the GOES-16 and -17 pairing and Himawari-8 paired with GOES-17. GOES-16 is stationed at 75.2°W (with fixed-grid reference longitude of 75°W) and GOES-17 is stationed at 137.2°W (with fixed-grid reference longitude of 137°W). Himawari-8 is stationed at 140.7°E with the same fixed-grid reference longitude. Dual-GOES coverage is possible over much of CONUS, while the GOES-Himawari pairing covers much of the Pacific west of Hawaii. This Pacific coverage is significant in light of the LHP anomaly onboard GOES-17, which renders height assignment problematic at certain times of day in certain seasons but leaves cloud-motion tracking possible with IR Band 14. In such circumstances, an operational GOES wind product with proper height assignments can be created from the GOES-Himawari pairing in the AHI-ABI overlap region where otherwise there would be none. Figure 1 also shows the overlap between GOES-16 and the future Meteosat Flexible Combined Imager (FCI) [22,23]. The FCI will have spectral channels, spatial resolutions, and FD coverage cadence similar to those of ABI, making FCI an excellent candidate for stereo winds over the Atlantic where hurricanes are spawned.

126

127
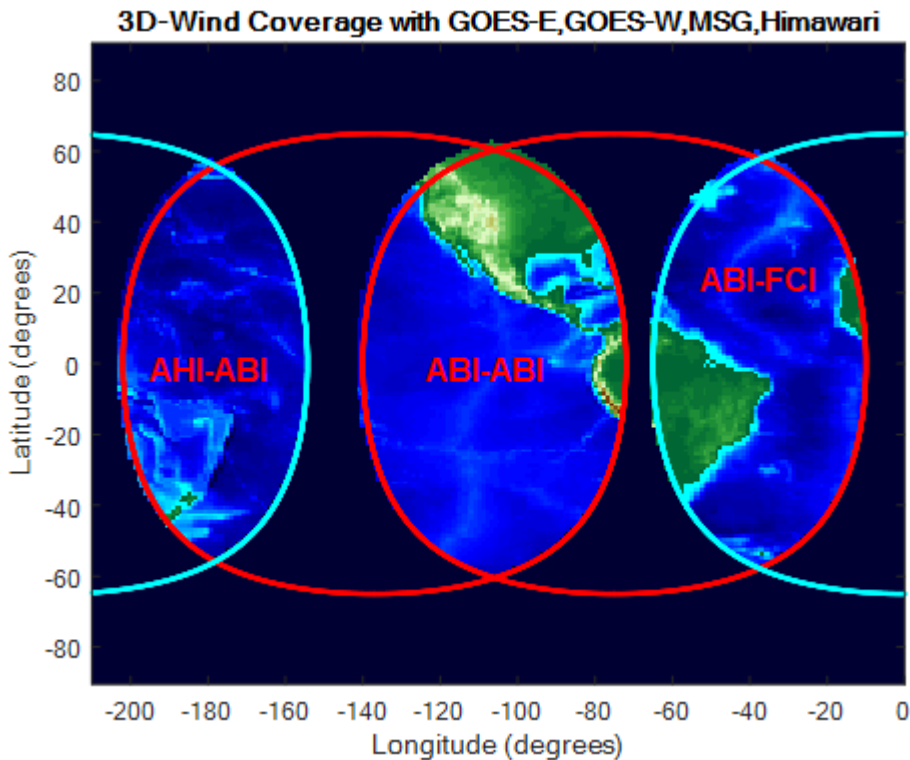
Figure 1. GEO-GEO stereo-wind products are possible in the overlaps between the coverage circles
of each GEO.   The circles drawn are limited to an Earth Central Angle (ECA) < 65° around the SSP
for each of the satellites.

2.2 GOES-GEO Stereo Winds Approach

Two GEO-GEO stereo-winds codes have been developed by the authors.   The NASA code is
implemented in MATLAB with some C-language plugins.   It has been scripted to run on the
Discover supercomputer at NASA's Goddard Space Flight Center (GSFC) to enable production of
large multi-day datasets.   GSFC has a local archive of GOES-R imagery that is easily accessed for
large production runs.   The NOAA code runs on a cluster at the NOAA Center for Satellite
Applications & Research (STAR) with local access to one year of GOES-R and Himawari datasets as
well as forecast background winds, and aircraft and rawinsonde observations.   It is implemented in
Fortran and uses the STAR Algorithm Processing Framework (SAPF) to enable its transition into an
operational context [24].   The NASA code is intended as a research tool to retrospectively process
cases of interest.   It allows for dense sampling of winds over designated geographic Regions of
Interest (ROIs).   The NOAA code is intended as a preoperational prototype for an Enterprise stereo-
winds product, as well as being a research tool, and it is integrated with legacy cloud analysis
capabilities.

Both codes follow the common approach diagrammed in Figure 2.   We designate one satellite
as the "A" satellite and remap the imagery from the other satellite ("B" satellite) into the fixed grid
of the A satellite.   The remapping uses Look-Up Tables (LUTs) giving the fixed-grid addresses of the
B-satellite pixels from which to form each pixel in the A-satellite's fixed grid.   Bicubic resampling
forms each remapped pixel from the neighboring pixels around the address in the LUT.   Target
templates are drawn from the middle repetition of a triplet of A satellite scenes (designated the "A0"
scene).   The targets are tracked in prior and forward repetitions of the A satellite's scenes ("A-" and
"A+") and in two repetitions of the remapped B satellite's scenes ("B-" and "B+") as shown.   The
NASA code uses simple assignment of template sites on a regular grid covering the A scene and
fixed-size templates.   We generally sample at half the template dimensions to effectively oversample

155   wind fields 2:1. The NOAA code inherits the tracer selection and nested tracking approach of
156   NOAA's operational Derived Motion Wind (DMW) product [8].   It takes advantage of the existing
157   DMW paradigm of processing scenes in triplets.   In application to stereo winds, two triplets are
158   processed: (A-, A0, A+) and (B-, A0, B+), both sharing the A0 scene from which the same tracking
159   templates are taken, and providing the rationale for the "K" diagram construction in Figure 2.
160
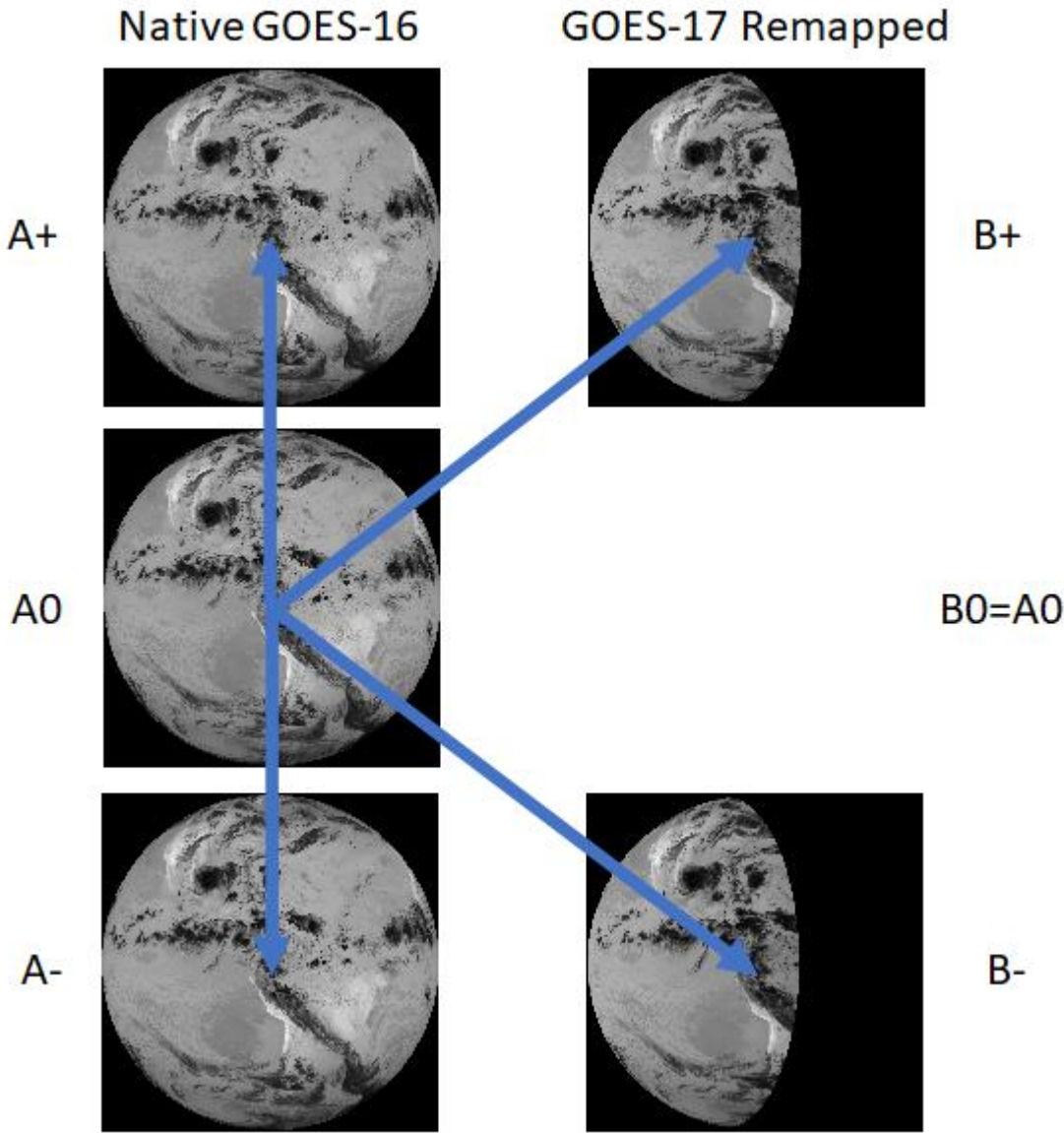
161
162   **Figure 2.** The GEO-GEO stereo-wind approach uses three A-satellite repetitions and two B-satellite
163   repetitions.   All repetitions of the A scenes must be the same scene type and the same for the B
164   satellite; however, A and B may be a different scene types (e.g., CONUS for A and FD for B).   In this
165   case, GOES-16 is the A satellite and -17 is the B satellite. The GOES-17 FDs have been remapped into
166   the fixed grid of GOES-16 leaving an area to the east where no remapped pixels could be constructed
167   since they are over the GOES-17 horizon.   Band 14 radiances are shown with arrow to indicate
168   matching for feature tracking with all templates taken from the A0 scene.

169   Pattern matching between A0 and A± reveals cloud or water-vapor feature motion, while
170   matching between A0 and B± reveals a combination of motion and parallax.   The retrieval model
171   unwraps the two and provides estimates of five states to describe the wind for each A0 site.   One
172   state is an altitude (h) for the tracked feature above the WGS-84 ellipsoid, two states represent a
173   horizontal position correction ($\vec{p}$), and the remaining two states represent a horizontal wind velocity

174   $(\vec{V})$.   We construct a local coordinate system at the ellipsoid site for each A0 template and resolve
175   vectors into (u, v, w)-components along the cardinal directions in the tangent plane (east along the
176   ellipsoid surface, north along the ellipsoid surface, and local vertical) as is shown in Figure 3.   The
177   states describe a displacement of the tracked feature in time from the fixed-grid position vector of the
178   A0 site on the ellipsoid $(\vec{r}_0)$ according to $\vec{\delta}$, where the vectors $\vec{p}$ and $\vec{V}$ only have components in the
179   (u, v)-plane and $t - t_0$ is the time assignment relative to the A0 template:
180
181   $$\vec{\delta}(t) = h\hat{w} + \vec{p} + \vec{V} \cdot (t - t_0). \tag{1}$$
182
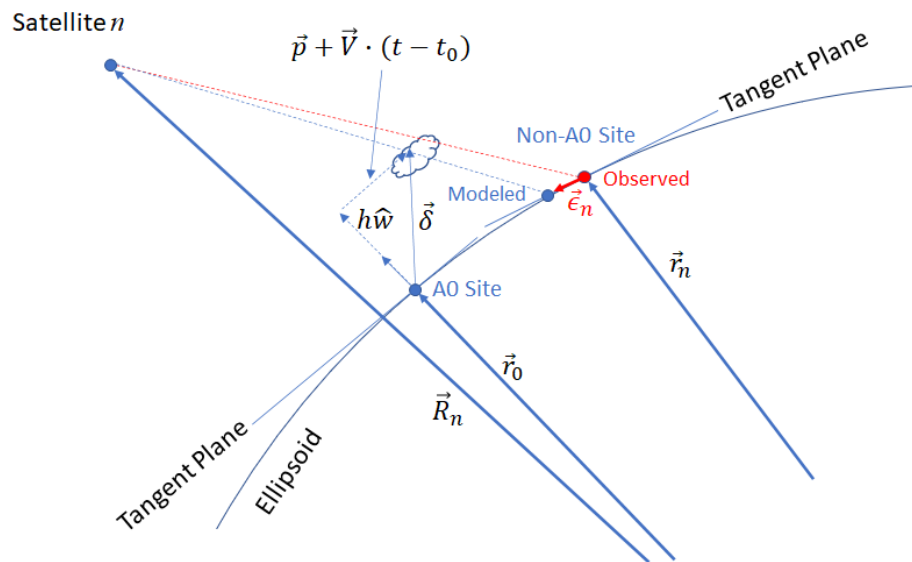
183
184   **Figure 3.** The states $X = (h, \vec{p}, \vec{V})$ model the position of the tracked feature, with the optimal state being
185   the one the makes the modeled distance from each observed site minimum in a least-squares sense.

186   Retrievals for the five states are attempted when there are four successful matches.   Each match
187   provides the ellipsoid locations for where the feature represented in the A0 template is found in the
188   A± and B± fixed grids under the assumption that a translation locally describes the change in the
189   feature between compared images.   The four apparent translation measurements are called
190   "disparities", borrowing the term from the field of computer vision.   Disparities are measured to
191   subpixel precision using interpolation in the feature matching process.   The NASA code uses
192   Normalized Cross Correlation (NCC) with interpolation on an NCC-coefficient surface [25] and the
193   NOAA code uses nested tracking based on a Euclidean norm measure of image similarity with
194   clustering of nested sub-template matches [8].   Therefore, each disparity measurement provides two
195   displacement components, for a total of eight measurements, from which to calculate the apparent
196   locations of the tracked feature on the ellipsoid as seen by each non-A0 satellite, $\vec{r}_n$ for $n \in$ {A-, A+,
197   B-, B+}.   We estimate the five states $X = (h, \vec{p}, \vec{V})$ by weighted least-squares minimization of the
198   distances in the tangent plane between the observed and modeled locations for the feature, $\vec{\varepsilon}_n =$
199   $\vec{\varepsilon}(\vec{r}_n, \vec{R}_n, t_n, X)$, across all four pairings with A0:
200
201   $$\chi^2 = \sum_n w_n |\vec{\varepsilon}_n|^2. \tag{2}$$
202

203   In general, not all $\vec{\varepsilon}_n$ can be simultaneously zero but only as close to zero as the weighted (w_n) least-
204   squares solution allows.   The state X that minimizes χ^2 is found iteratively by nonlinear
205   optimization since χ^2 is mildly nonlinear in X.   The retrieval process just described was first used
206   in our previous work with MISR-GOES [10] and then with MODIS-GOES stereo winds [11].   A full
207   derivation of the least-squares solution is provided in the Appendix of the MISR-GOES paper.   It
208   includes a coupling between problem states at different sites to represent systematic errors between

209 the MISR and GOES imagery. In the GEO-GEO problem, the solutions at different sites are
210 independent of each other.
211 The residuals assuming the estimated state X_0, $\vec{\varepsilon}_n(X_0) = \vec{\varepsilon}(\vec{r}_n, \vec{R}_n, t_n, X_0)$, provide a measure of
212 how well the disparities are explained by the retrieval model. Plots across of $\vec{\varepsilon}_n(X_0)$ across the
213 population of all retrievals (Figure 4) can reveal small systematic error signatures and anomalous
214 cases where the model does not explain the data. We mark anomalous retrievals with a Data Quality
215 Flag (DQF) to indicate a poor retrieval. Anomalous cases are identified statistically, with a gross-
216 error test with a fixed threshold on each $\vec{\varepsilon}_n$, an optional Median Absolute Deviation (MAD) filter on
217 the collection of all $\vec{\varepsilon}_n$, or the first followed by second.

218
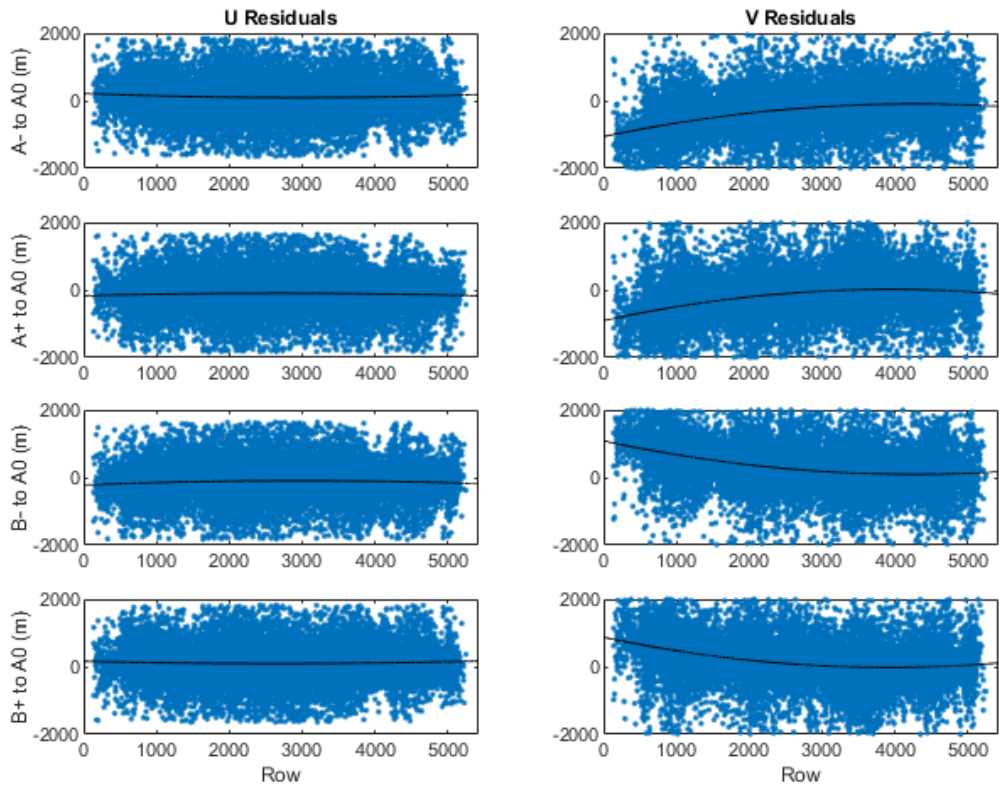
219 **Figure 4.** Residuals for an ABI-AHI FD pair shows the signature of a small of systematic error in the
220 Band 14 imagery for Himawari in relation to that of GOES-17. Least-squares second-degree fits are
221 over-plotted. For context, an IR resolution element is 2 km at SSP.

222 Our organization of the processing into two matching steps in triplets (A-, A0, A+) and (B-, A0,
223 B+) is convenient with respect to adding stereo capabilities to NOAA's operational wind product
224 codes; however, alternative schemes are also possible. Our MODIS-GEO stereo-winds code, with
225 GEO meaning either GOES-R or Himawari, works according to a different scheme. It gathers
226 matches from an (A-, A0, A+) triplet and matches between A0 and a sequence of MODIS granules
227 remapped into the A-satellite fixed grid. This scheme provides six measurements for each five-state
228 retrieval, which is still overdetermined, but less so and hence less robust. This would be analogous
229 matching from an (A-, A0, A+) triplet and adding a B0-A0 pair. If the A and B satellite image
230 acquisition were synchronized, the B0-A0 pairing would reveal only parallax, which would be an
231 advantage. However, the construction of the retrieval model with an explicit reference to time in
232 Equation (1) allows its use where image acquisitions by the two satellites are not synchronized. The
233 MODIS-GEO and MISR-GEO applications are two examples. Also allowed is a CONUS frame from
234 one GOES-R satellite paired with the FD from another satellite. We discuss pixel times next,
235 knowledge of which enables our algorithm to work without synchronizing the observing systems.

236   *2.3 Pixel Time Tags*

237   Time-tag metadata for individual ABI pixels are not provided with the ABI Level-1 product, but
238   time metadata are provided within the AHI product files [26].   We can derive the AHI pixel times
239   directly from this temporal metadata, but ABI pixel times must be modeled considering the ABI
240   observational mode and timeline version.   Figure 5 is an example of an ABI Mode 6 timeline showing
241   the schedule of activities that ABI conducts within a 10-minute period.   It consists of a single
242   repetition of the FD, two repetitions of a CONUS, and 10 MESO repetitions.   The ABI FD is covered
243   in 22 scan swaths, the CONUS is covered in six scan swaths, and each MESO is covered in two back-
244   to-back swaths.   The ABI product time indicates the time of the first Band 2 detector sample used to
245   form the product.   We add an offset from our ABI pixel time model and an adjustment for the
246   spectral band to account for the in-field separation of the detectors of different spectral channels
247   relative to centerline of the focal planes.   The time models consist of a LUT for each 2-km pixel in
248   each scene and are included in the supplementary materials accompanying this paper as files in
249   network Common Data Form (netCDF).   The time-model LUTs will require revisions as different
250   timelines are defined and used operationally and possibly when there are new releases of the ground
251   Level-1 processing software.   Our method for creating the time-model LUTs is described in the
252   Appendix.

253

254
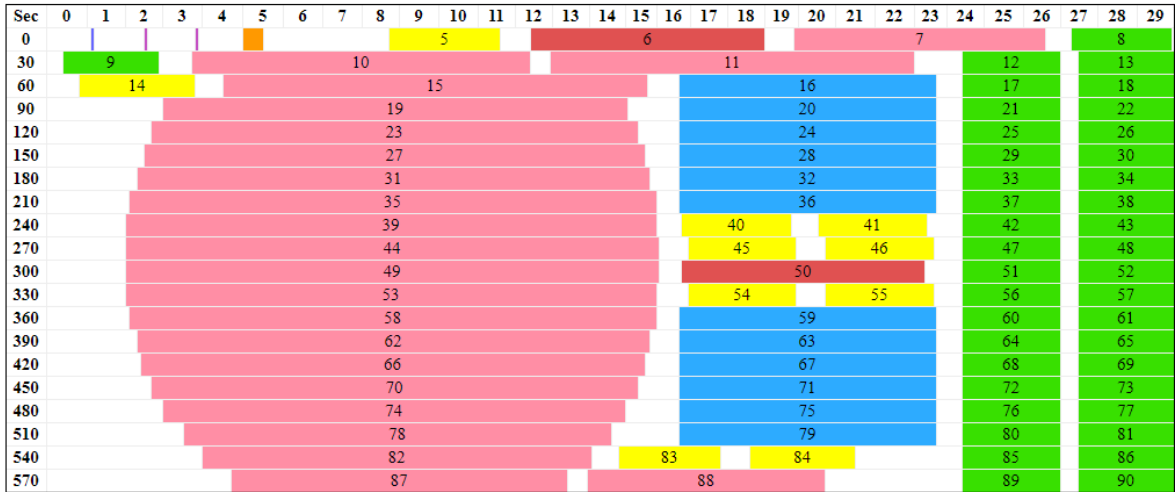
255   **Figure 5.** A GOES timeline for ABI Mode 6 (version 5B) shows twenty 30-second segments in which
256   22 swaths (salmon) complete one FD, six swaths (blue) make each of two CONUS scenes, and 40
257   swaths (green) make either one or two MESO scenes.   Other activities such as calibrations and star
258   acquisitions are also shown.

259   A time t_0 is assigned to a template at its center pixel and times t_n at the sites for each match
260   rounded to the nearest pixel.   These time assignments are used in the retrieval process as described
261   in Section 2.2.   An example from a CONUS-FD case is shown in Figure 6, where time tags are plotted
262   versus the row number in the A0 scene (in this case, GOES-16 CONUS).   The pixel times for the B
263   satellite (GOES-17 in this example) are first modeled in the B-satellite fixed grid and then remapped
264   along with B-satellite imagery so that they may be indexed in the fixed grid of the A satellite.
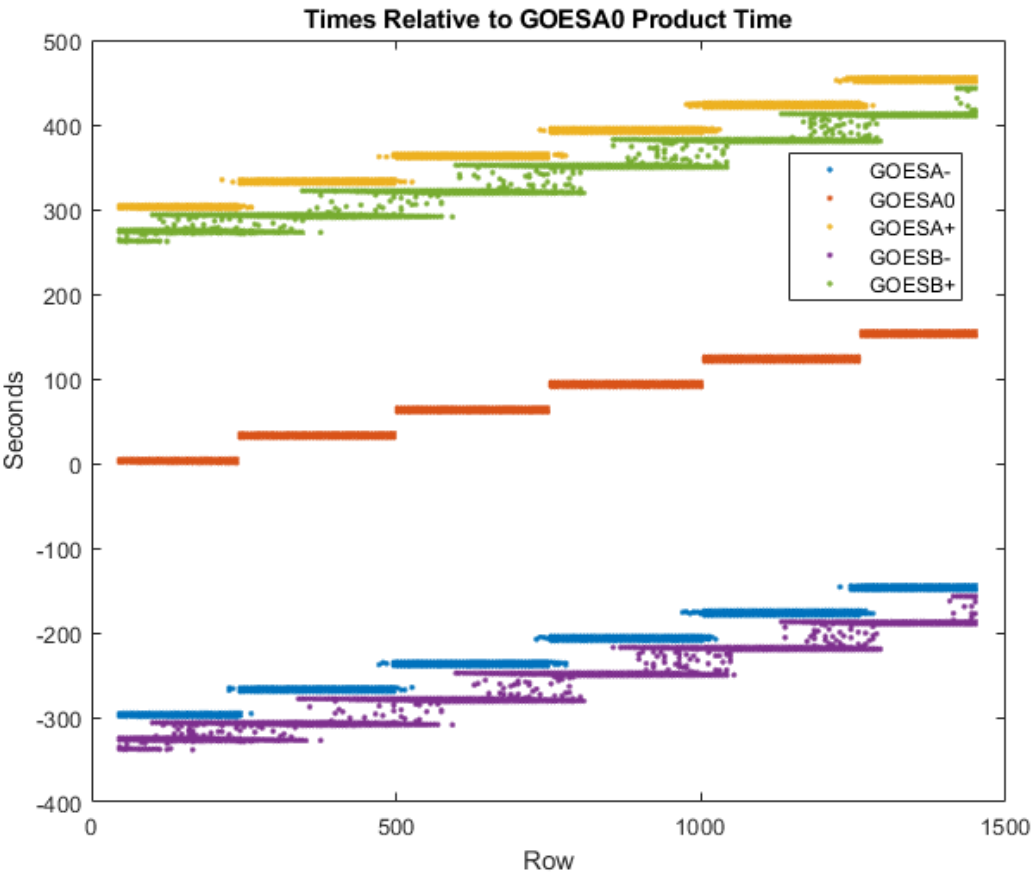
Figure 6. Assigned times for a CONUS-FD Band 14 case during Hurricane Hanna (A0 GOES-16 CONUS time: 2020/207 17:16Z). Time generally progresses as the row number increases from north to south. Swath transitions are evident as a staircase. The two FDs from GOES-17 fall close to the A± CONUS repetitions from GOES-16, which are the first CONUS repetitions in their respective timelines and the A0 scene is the second repetition of the CONUS scene within its timeline.

2.4 Spacecraft Position Vectors

Spacecraft position vectors are also required for each retrieval. These are quasi-static in a geographic reference frame. We use the assigned satellite stations for GOES-16 and -17 (75.2°W and 137.2°W) and assume they are on the equator with a nominal orbital radius of 42164.17478 km. These locations will be accurate to <0.1° depending on the timing within the GOES station-keeping cycle. For Himawari, metadata giving an SSP latitude and longitude and the orbit radius for the scene is provided in the AHI product files [26], which we use directly.

2.5 Divergence and Curl

The NASA code includes the calculation of the divergence and curl of the retrieved wind fields. Similar upper-level wind-field divergence products have used operational 6.2-µm AMV data [27,28]. The cloud-top divergence derived from AMVs is a result of the outflows from storm updrafts that can be used to diagnose the updraft intensity and associated precipitation at the surface. The operational divergence product is limited to the 6.2-µm channel (similar to Band 8 in the GOES-R series), because this channel has a roughly uniform weighting function with respect to water vapor (WV). In other words, the height associated with the 6.2-µm AMVs is at the approximately same level, which is required to calculate the wind field divergence. However, one can derive the divergence and curl from the wind field in every channel where there are sufficiently dense retrievals in clearly identifiable layers. In the NASA code, the calculations of divergence and curl are performed at the

289 site of each retrieval with nominal DQF by considering all the retrievals within a horizontal spatial
290 window and within the same layer as determined by a vertical window.   We work with the
291 Cartesian (u, v, w) -coordinates constructed as described in Section 2.2 above, with (u, v) as
292 coordinates for the tangent plane at the site central to the neighborhood.   If sufficiently many, well
293 distributed neighboring retrievals are found within the spatial window, the neighboring wind
294 vectors are fit as functions of their sites' (u, v)-coordinates.   All winds in the fit are regarded as
295 belonging to the same atmospheric layer and therefore assumed to share the same vertical w-
296 coordinate.   The divergence and curl are computed from the vector field described by this fit.   A fit
297 is attempted only when the horizontal spatial window is ≥25% populated by neighboring retrievals
298 with nominal DQFs, all four quadrants have ≥5% of their possible sites populated, and the retrieved
299 wind at the central site is part of the main layer (generally within ±1 km of the median for the window).
300 The fit is in the form of a polynomial in local Cartesian coordinates (u, v) with degree three in each
301 variable (i.e., bicubic).   The total and quadrant population tests are necessary to adequately constrain
302 the fit.   The fit is performed as a linear least squares problem with 6-sigma MAD filtering to discard
303 statistical outliers.   The fit is redone until either until no more data are discarded, or the population
304 criteria fail.   We fit the wind retrievals after the central wind (retrieval at the site) is subtracted from
305 all neighboring winds, which does not affect the spatial derivatives.   With the central wind removed,
306 we can skip the constant term and fit the retrieved winds to a nine-parameter model that solves for
307 the 2x9 coefficient matrix A in the model representation:

$$\vec{V}(u, v) = A \cdot [u \ \ v \ \ u^2 \ \ uv \ \ v^2 \ \ u^3 \ \ u^2v \ \ uv^2 \ \ v^3]^T + \vec{V}(0, 0). \tag{4}$$

311 Therefore, the wind-field fit represents the central wind at the site and differentiable changes
312 surrounding it.   The divergence and curl are computed from the fit coefficients:

$$div \ V = \left(\frac{\partial V_u}{\partial u} + \frac{\partial V_v}{\partial v}\right)_{u=v=0} = A_{u1} + A_{v1}, \tag{5a}$$

$$(curl \ V)_w = \left(\frac{\partial V_v}{\partial u} - \frac{\partial V_u}{\partial v}\right)_{u=v=0} = A_{v1} - A_{u2}. \tag{5b}$$

318 Only the vertical component of the curl is nonzero since all winds belong to the same layer.
319 Since we are working in the local Cartesian frame attached to the Earth, it is not inertial, and the curl
320 represents the relative vorticity.   The units of divergence and curl are both inverse time.
321 The wind-field fitting domain can be defined as an input with units of template sizes.   As the
322 domain enlarges with respect to the template, the derived divergence and curl becomes more
323 spatially averaged and larger values are averaged down.   Since mesoscale severe weather would be
324 a primary application for these derived quantities, smaller domains should be preferred, but the
325 domain must be large enough to represent the spatial variation of the retrieved wind field
326 (oversampled winds will correlate neighboring retrievals because their templates overlap).
327 The divergence and curl of the retrieved wind field are included in the netCDF output file of the
328 NASA code along with the retrieved wind velocities, their assigned heights above the WGS-84
329 ellipsoid, the geoid height above the ellipsoid and terrain height above the geoid at the retrieval sites,
330 and data quality flags.   Some applications for these derived wind fields are found in Section 3.3.

3. Results

332 In principle, stereo winds can be made from any GOES spectral channel or any pairing of similar
333 channels in a mixed constellation.   In this section, we feature results from the ABI reflective Bands 2
334 and 4, Water Vapor (WV) Bands 8, 9, and 10, and window-IR Band 14.   It should also be possible to
335 use synthetic bands formed from channel differences, ratios, or spectral indices that enhance
336 characteristics such as atmospheric composition or dust.   We will use the abbreviation "B02", "B04",
337 etc. to identify the spectral bands.

338   Our first results, in Section 3.1, pertain to validation of the method.   Section 3.2 investigates the
339   error characteristics of stereo winds and their height assignments.   Section 3.3 provides stereo-wind
340   retrievals that address several application areas where the simultaneous retrieval of wind height is
341   likely to provide some advantages with respect to conventional IR wind height assignments in
342   addition to providing high-quality height assignments for assimilation into numerical weather
343   models.   These include studies of deep convection in tropical cyclones, observation of the Planetary
344   Boundary Layer (PBL), and smoke plumes from wildfires.

345   *3.1 Validation*

346   Our validations include tracking stationary ground points under clear-sky conditions and
347   comparisons to rawinsonde observations and the NOAA operational wind algorithm.   The ground-
348   point retrievals provide an indication of the accuracy of the stereo retrievals.   The rawinsonde results
349   show the potential benefits of stereo winds relative to operational winds where both exist.

350   3.1.1 Ground point retrievals

351   The NASA code is indiscriminate in its selection of features to track and will track static
352   ground points as if clouds borne in the wind.   We know the velocities (zero) and elevations of
353   tracked ground points from terrain models to compare against the retrievals.   This method has
354   been pioneered with MISR [29] and applied in our work in LEO-GEO stereo winds.   We use a
355   similar methodology [10] to identify the class of candidate ground-point retrievals by a combination
356   of height above ground level and low speed.   Statistics over this class are useful for characterizing
357   retrieval errors even if the problem of tracking a cloud in motion may be different than tracking
358   static terrain as noted by Lonitz and Horvath [30].   Figure 7 shows the statistics of ground-point
359   retrievals using a pair of GOES-16 and -17 FDs in B14; also shown are the derived divergence and
360   curl at these sites.   Figure 8 shows the ground-point retrievals for the same scene pair in B02.   A
361   visual inspection of the sites that have been classified as ground points confirms the correctness of
362   their classification, although this is more difficult for IR scenes.   The counts are higher for B02 than
363   B14 both because there are more retrieval sites available and because the smaller footprint of the
364   B02 templates allows for more clear-sky conditions to be found.   As expected, the error statistics
365   are also smaller in B02 than B14 due to the finer precision offered for tracking with a finer spatial
366   resolution.   B14 may include some templates contaminated by low clouds.   Evidence of
367   bimodality is seen in the B02 velocity histogram. This cluster of ground-point retrievals are
368   concentrated over the Andes.   These are most likely traceable to an INR error in the southern
369   portion of the FD.
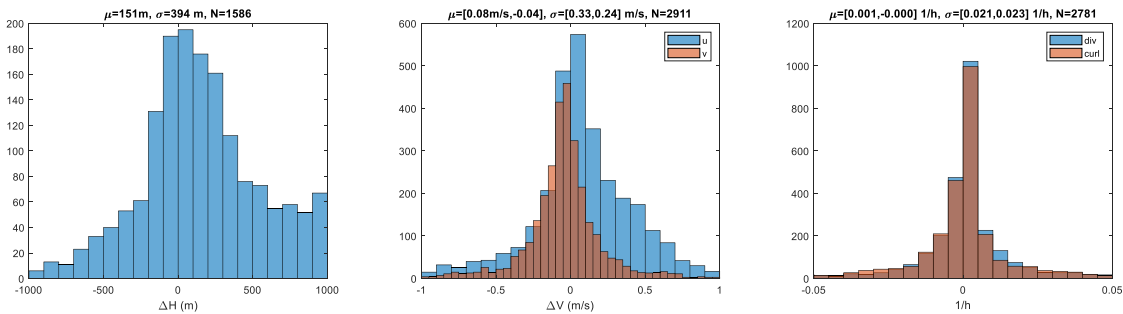
371   **Figure 7.** Ground-point retrievals in B14 at 2020/207 17:20Z from GOES-16 and -17 FDs using a 24x24
372   pixel template and 12x12 pixel sampling.

Figure 8. Ground-point retrievals in B07 at 2020/207 17:20Z from GOES-16 and -17 FDs using a 24x24 pixel template and 12x12 pixel sampling.

A larger collection of ground-point statistics have been gathered from our runs on the NASA Discover supercomputer. These are collected by case and summarized in Table 2. These large samples indicate retrieval errors are ~0.1 m/s for B02 AMVs, ~200 m for B02 heights, ~0.2 m/s for IR AMVs, and ~250 m for IR heights. Tracking clouds in motion is a slightly different problem and may have different error characteristics; however, these results should still be indicative of the expect accuracy of stereo methods. All cases used 24x24 pixel templates and a GOES-16 CONUS and a GOES-17 FD.

Table 2. Ground-point mean (μ) and standard deviation (σ) statistics are presented for cases run on the NASA Discover supercomputer indicate the uncertainties in stereo-winds retrievals.

Case	Start	Band	N	Height (m)		u-Wind (m/s)		v-Wind (m/s)	
	Stop			μ	σ	μ	σ	μ	σ
Western Orographic	26 July 2019 17Z	2	1,184,516	-8.3	96.3	-0.03	0.06	-0.03	0.07
	-	7	82,832	24.6	184.8	-0.02	0.11	-0.05	0.12
	26 July 2019 23Z	14	34,733	76.4	176.7	-0.01	0.11	-0.03	0.12
Hanna	21 July 2020 5Z	2	752,841	13.1	108.6	-0.02	0.08	-0.03	0.08
	-	7	176,125	26.8	205.1	-0.03	0.13	-0.04	0.13
	29 July 2020 17Z	14	41,157	125.3	208.9	-0.04	0.14	-0.03	0.15
Imelda	17 Sep 2019 5Z	2	588,193	-3.4	84.0	-0.02	0.08	-0.03	0.08
	-	7	520,547	-7.2	171.4	-0.01	0.13	-0.03	0.12
	23 Sep 2019 17Z	14	245,513	50.7	195.5	-0.01	0.14	-0.03	0.14
Creek Fire	8 Sep 2020 12Z	2	3,615,312	6.2	172.7	-0.01	0.09	-0.04	0.10
	-	7	491,027	4.2	230.8	-0.01	0.12	-0.05	0.12
	13 Sep 0Z	14	455,228	29.1	234.1	-0.01	0.12	-0.06	0.12

3.1.2 Rawinsondes

The NOAA code has access within its run environment to both rawinsonde observations and forecast winds from NOAA's National Centers for Environmental Prediction (NCEP) Global Forecast System (GFS) against which to validate and compare with stereo-wind retrievals. GOES-17/GOES-16 stereo winds and NOAA operational GOES-17 B14 Full Disk winds at 0Z and 11Z were each compared to coincident (within approximately 100km and 60 minutes) 0Z and 12Z rawinsonde observations. The 11Z stereo and operational winds were chosen to be collocated with the 12Z rawinsonde observations since the GOES-17 ABI Loop Heat Pipe (LHP) anomaly [15,16] resulted in the generation of very few operational winds at 12Z during the month of April 2020. The stereo and operational winds were generated for the same times and were required to be within approximately 10 km of each other, thus ensuring a one-to-one comparison of the performance between the two using the same rawinsonde observations as "truth". Table 3 shows the overall (i.e., winds at all levels and at all latitudes) comparison statistics in tabular form between rawinsonde winds (0Z and 12Z) and GOES-17/GOES-16 stereo winds, NOAA operational GOES-17 winds, and GFS 12-hour

399 forecast winds for April 1-30, 2020. The comparison metrics are those described in the World
400 Meteorological Organization (WMO)/Coordination Group for Meteorological Satellites (CGMS)
401 guidelines for reporting the performance of satellite-derived winds [31]. The Mean Vector Difference
402 (MVD) is computed from:
403
404 $$MVD = \frac{1}{N}\sum_{i=1}^{N}(VD)_i \qquad (6a)$$
405 where
406 $$(VD)_i = \sqrt{(u_i - u_r)^2 + (v_i - v_r)^2} \qquad (6b)$$
407 and
408 $u_i =$ u-component of satellite wind,
409 $v_i =$ v-component of satellite wind,
410 $u_r =$ u-component of the collocated reference wind,
411 $v_r =$ v-component of the collocated reference wind, and
412 $N =$ size of collocated sample.
413
414 The average speed bias between the satellite and GFS model winds or rawinsonde reference
415 winds is computed from:
416
417 $$(BIAS)_i = \frac{1}{N}\sum_{i=1}^{N}\left(\sqrt{u_i^2 + v_i^2} - \sqrt{u_r^2 + v_r^2}\right) \qquad (7)$$

418 **Table 3.** Comparison statistics between rawinsonde winds (0Z, 12Z) and GOES-17/GOES-16 stereo
419 winds, NOAA operational GOES-17 winds, and 12-houir forecast winds for April 1-30, 2020.

All Levels, Latitudes	GOES-17/GOES-16 Stereo Winds	NCEP GFS 12hr Forecast Winds
Mean Vector Difference (m/s)	4.79	4.46
Speed Bias (m/s)	-1.09	-0.28
Average Speed (m/s)	22.33	23.14
Absolute Direction Difference (deg)	10.46	10.05
Sample Size	17,999	17,999
All Levels, Latitudes	GOES-17 Operational Winds	NCEP GFS 12hr Forecast Winds
Mean Vector Difference (m/s)	4.97	4.27
Speed Bias (m/s)	-0.79	-0.33
Average Speed (m/s)	22.34	22.81
Absolute Direction Difference (deg)	10.76	9.62
Sample Size	17,999	17,999

420
421 The overall comparison statistics (Table 3) show that the GOES-17/GOES-16 stereo winds have
422 better quality than the NOAA operational GOES-17 winds as measured by their respective MVDs
423 (4.79 m/s versus 4.97 m/s).   The quality of the stereo winds also more closely approaches the quality
424 of the GFS model forecast winds than the operational winds as represented by the smaller differences
425 in MVD with respect to the forecast. It is important to point out that the height assignment differences
426 associated with the stereo and operational winds are what is driving the differences between the
427 comparison statistics for the stereo and operational winds. There are very small differences between
428 the speeds and directions associated with the stereo and the operational winds since the same feature
429 tracking algorithm is used to derive both. The mean speeds of the stereo and operational winds in
430 Table 3 are virtually identical which is clear evidence of this. The stereo wind height assignments are
431 based on cloud heights derived via the stereo model described above in Section 2.2. The height
432 assignments associated with the operational winds are based on cloud heights derived using an
433 infrared based retrieval algorithm [32,6].

434   The overall comparison statistics in Table 3 do not reveal the whole story about the error
435   characteristics of the satellite winds. To do this, we generated Figure 9 which illustrates vertical
436   profiles of MVD (triangles) and speed bias (satellite wind – rawinsonde; squares) comparison metrics
437   for the GOES-17/16 stereo winds (blue) and NOAA operational winds (red) at 00 and 12Z for April
438   1-30, 2020. The comparison metrics are computed over 100 hPa layers. The corresponding sample size
439   vertical distributions are shown in the bottom three panels. Most of the collocations are found at
440   upper levels of the atmosphere with a peak around 250 hPa with decreasing numbers of collocations
441   at lower levels. The combined comparison statistics at 0Z and 12Z (top left panel) indicate that the
442   quality of the stereo winds at all levels is as good or better than the quality of the operational winds.
443   The exception is in the 500–800 hPa layer, where the magnitude of the speed bias (satellite wind –
444   rawinsonde wind) is larger for the stereo winds. A comparison of the vertical distribution of counts
445   at 0Z (bottom middle panel) suggests some of the low-level winds may be assigned incorrectly to
446   mid-levels by the stereo method which explains the larger speed bias for the stereo winds. We see
447   this behavior more at 0Z (top middle panel) than at 12Z (top right panel) for which we do not have a
448   clear explanation. At upper levels of the atmosphere, which has the highest population of measured
449   winds, the stereo winds exhibit higher quality than the operational winds more clearly. At these
450   levels of the atmosphere, thin cirrus clouds dominate the sample and present the largest challenge to
451   the operational infrared-based cloud height retrieval algorithm [32,6]. Unlike this infrared-based
452   cloud height retrieval approach, the stereo approach does not rely on cloud microphysical properties
453   or explicit knowledge of the atmospheric thermal structure to estimate cloud heights. As such, the
454   stereo approach generates very accurate cloud heights for wind tracers associated with thin cirrus
455   regimes and this result clearly benefits the quality of the upper-level stereo winds. This is especially
456   true at 12Z (top right panel) when the operational cloud height algorithm is further challenged by the
457   loss of ABI water vapor and CO_2 band imagery due to the GOES-17 ABI Loop Heat Pipe (LHP) issue.
458   In this situation, the operational cloud height algorithm only uses ABI B14 to retrieve cloud heights
459   that results in retrieved cloud heights that are too low in the atmosphere for thin cirrus clouds. The
460   quality of the operational winds that use these cloud heights is seriously compromised. To more
461   clearly illustrate this point, Figure 10 shows a time series of the MVD comparison statistics for the
462   upper level operational and stereo winds at 0Z and 12Z for the month of April 2020. Note the much
463   lower MVD values for the stereo winds at these times throughout April which clearly indicate that
464   their quality is much better than the operational winds. Also plotted in Figure 10 is the time series of
465   the GOES-17 ABI Focal Plane Module (FPM) temperatures that show that the ABI instrument warms
466   anonymously between 12 and 18Z of each day during April. It is during these times of the day when
467   the operational winds quality and counts are most impacted. Note the larger separation between the
468   MVD curves during days (~ April 14-23, 2020) when the peak ABI FPM temperatures are their
469   warmest. It is during this time period that the quality of the stereo winds is significantly better than
470   the quality of the operational winds.

471
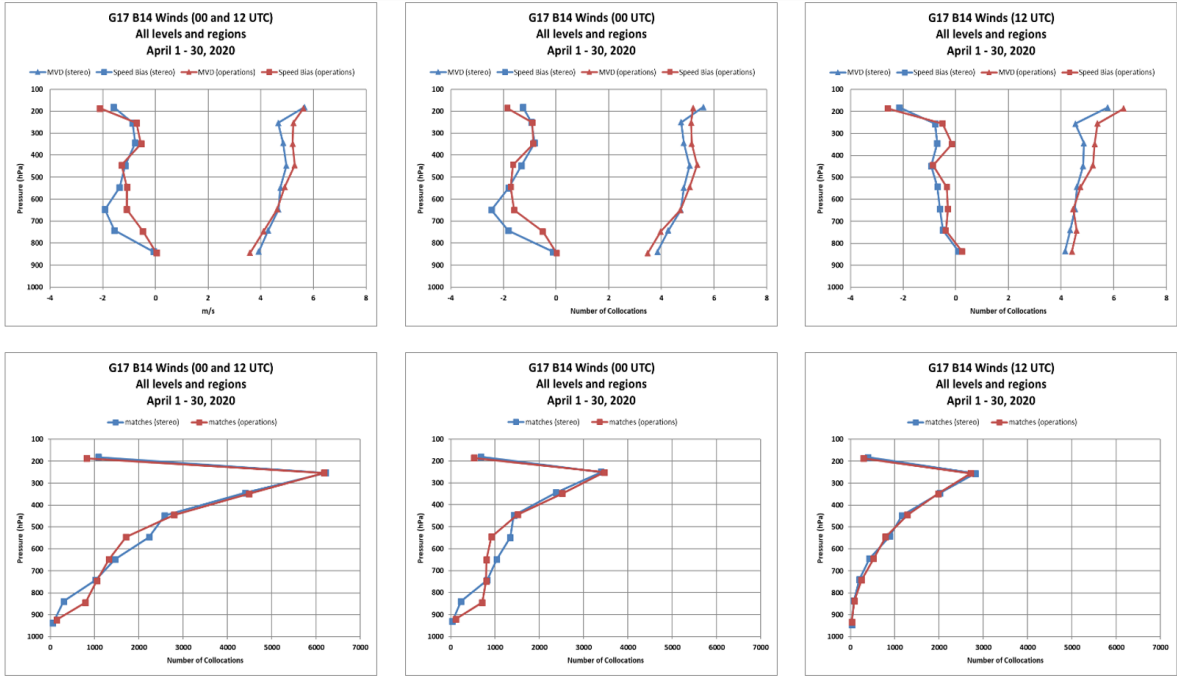
Figure 9. Vertical profiles of MVD (triangles) and speed bias (satellite wind – rawinsonde; squares)
for GOES-17/16 stereo winds (blue) and NOAA operational winds (red) at 00 and 12Z, 0Z, and 12Z
for April 1-30, 2020 are shown in the top three panels. The corresponding number of collocations are
shown in the bottom three panels.

476
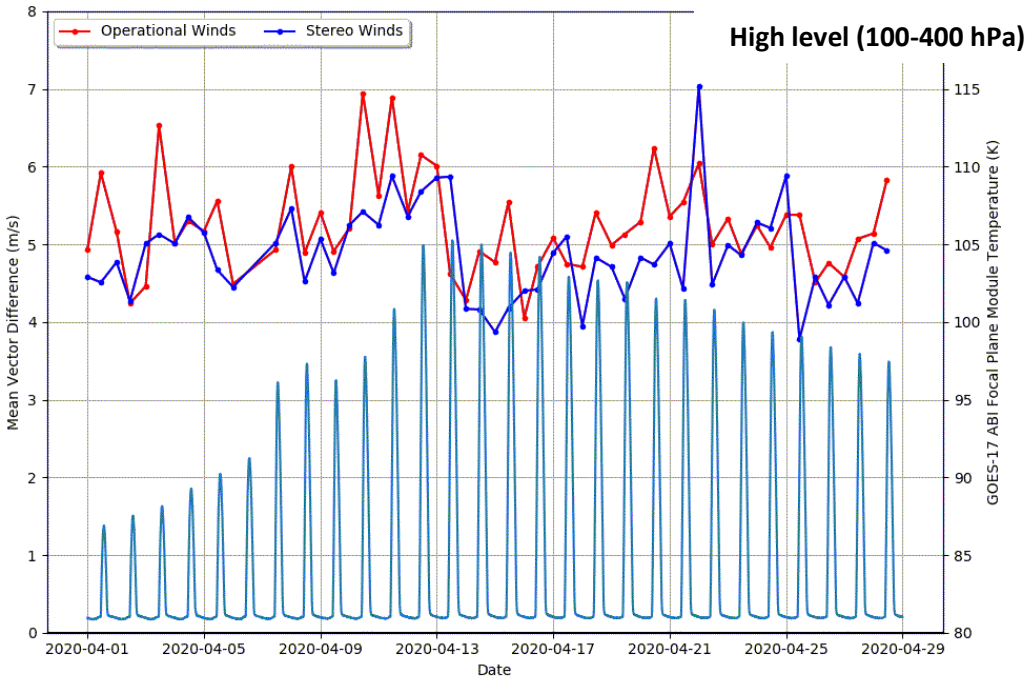
Figure 10. Time series of the Mean Vector Difference for upper level (100 – 400 hPa) stereo winds
(blue) and NOAA operational winds (red) along with the time series of the GOES-17 ABI Focal Plane
Module (FPM) temperatures (light blue) for April 1-30, 2020.

3.2 Statistics of Stereo Height and Winds

The stereo method can be applied to both cloud and water vapor features.

482   3.2.1 Cloud Features

483   Each ABI spectral channel may feature different cloud layers due to their different sensitivities
484   to cloud reflectivity, emission, and scattering. Four spectral channels (two reflective and two emissive)
485   are used to illustrate the distribution differences of stereo-height retrievals (Figures 11 and 12) from
486   the NASA code. The red-band visible channel (B02) retrieves stereo heights at all levels with the
487   majority of measurements at low levels, because cirrus clouds have poorer contrast in the presence
488   of low-level clouds. On the other hand, the reflective Short-Wave IR (SWIR) 'cirrus band' (B04) is
489   sensitive mostly to daytime high-level clouds due to the strong water vapor absorption in this band.
490   Unless the upper troposphere is very dry, low-level clouds are 'invisible' or featureless in B04. The
491   vertical distributions of stereo-height retrievals from these two bands reflect their differences in
492   sensitivity. As seen Figure 11, most of the oceanic PBL clouds in B02 retrievals are not present in B04,
493   while a significant number of high clouds are reported by B04 at high latitudes and over landmasses.
494   Cirrus anvil outflows in the tropics and above the mid-latitude jet stream overwhelm the B04
495   retrievals in comparison with B02. In the southeastern Pacific where the downwelling branch of
496   Hadley circulation produces a dry upper troposphere, both B02 and B04 retrievals yield a large
497   amount of low-level clouds over the marine PBL. Compared with Band 4, B02 has advantage of
498   observing smaller spatial cloud structures and can track these features at a lower altitude more
499   readily in a broken cloudy scene because of its finer resolution.
500   The Mid-Wave IR (MWIR) B07 and Long-Wave IR (LWIR) B14 channels have good sensitivity
501   to both high and low-level clouds, but their sensitivity to cirrus is significantly better than B02. The
502   different balance between high and low clouds is evident in the maps (Figure 11) and zonal mean
503   height statistics (Figure 12). Despite the same pixel resolution, B14 generally produces more stereo-
504   height retrievals than B07, which is consistent with the results found in the MODIS-GOES 3D-wind
505   study [11]. In addition to the high and low-level clouds, a distinct cloud type can be retrieved from
506   the stereoscopic technique, that is tropical congestus cloud in the mid-troposphere (Figure 12). As
507   summarized in a comparative study of different cloud remote sensing techniques [33], congestus
508   clouds are often smeared out with the IR-based height assignment, as opposed to stereoscopic and
509   lidar techniques. The ability of detecting congestus clouds has an important implication for
510   understanding atmospheric instability and convection development.
511   The combined sampling from the four spectral bands can fill the altitude gaps of AMV
512   measurements. As revealed in Figure 12, B02 has a wide coverage of low-level winds while Bands 4,
513   7 and 14 help to fill the mid- and upper-tropospheric winds. For global data assimilation (DA)
514   systems, this improved vertical sampling would increase the impacts of AMV measurements in the
515   mid-troposphere. With a better height assignment for low-level clouds, as suggested in Observing
516   System Experiments (OSE) studies [34,35], more AMVs in PBL would reduce global moisture energy
517   error in the DA systems. In the East Pacific and America sector, the zonal mean AMVs reveal two
518   eastward upper-tropospheric jets at mid-to-high latitudes and a weak westward flow in the tropics.
519   These zonal means are biased to cloudy atmosphere, showing that the jet in the SH (~40 m/s in the
520   zonal wind) is stronger than one in the NH. The meridional winds within the jets appear to have a
521   reversal at ~8 km in the SH and ~9 km in the NH, with a poleward flow below and an equatorward
522   flow above that altitude. In the tropics the intertropical convergence zone (ITCZ) is characterized by
523   several converging and diverging latitude bands in the upper troposphere, and a converging band at
524   10°N in the PBL. For all these features, the 3D-wind algorithm demonstrates the vertical resolution
525   needed to study the dynamics and their structural evolution with time.

526
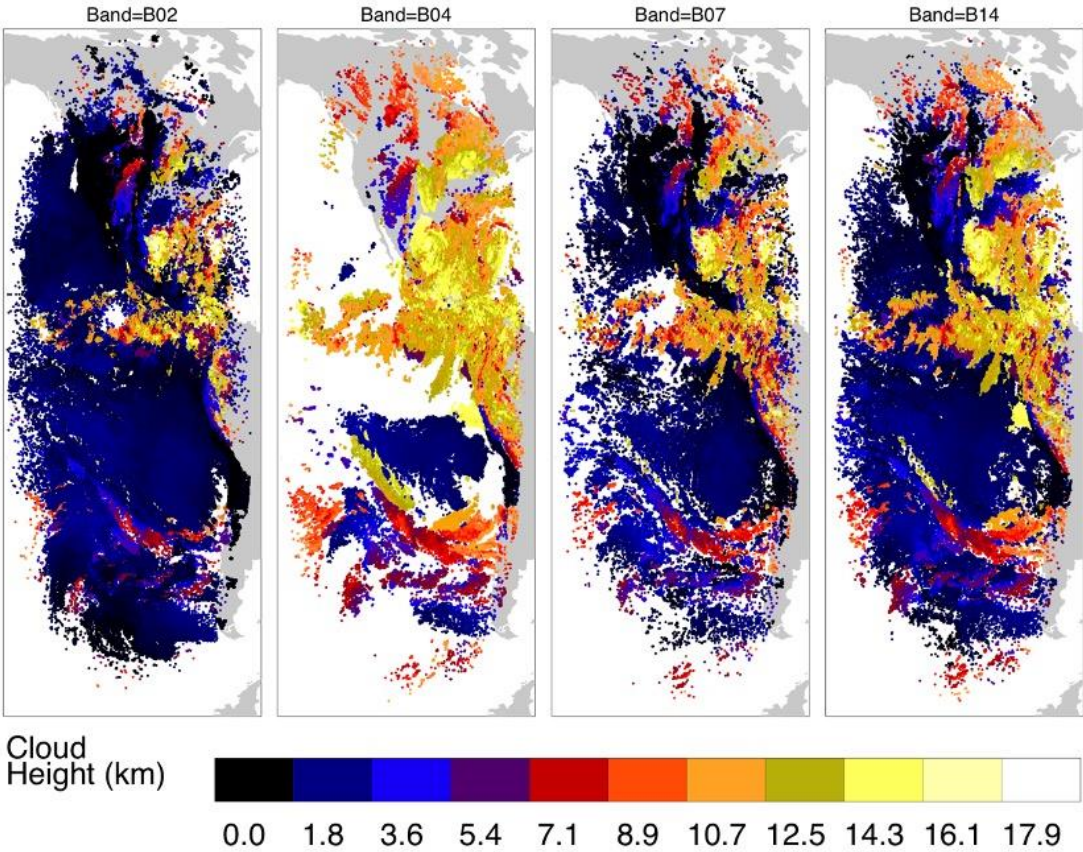
Figure 11. Spatial distribution of FD-FD cloud height retrievals from four GOES-16 and -17 spectral bands on 25 July 2020, 17:20Z when Hurricane Hanna is evident in the Gulf of Mexico. A 12x12 pixel chip size and 6x6 pixel sampling size are used in the retrieval configuration. A total of 103744, 97030, 110505 and 146571 good retrievals are produced for Bands 2, 4, 7, and 14, respectively, whereas B02 has a 4x better resolution than the other bands.

534
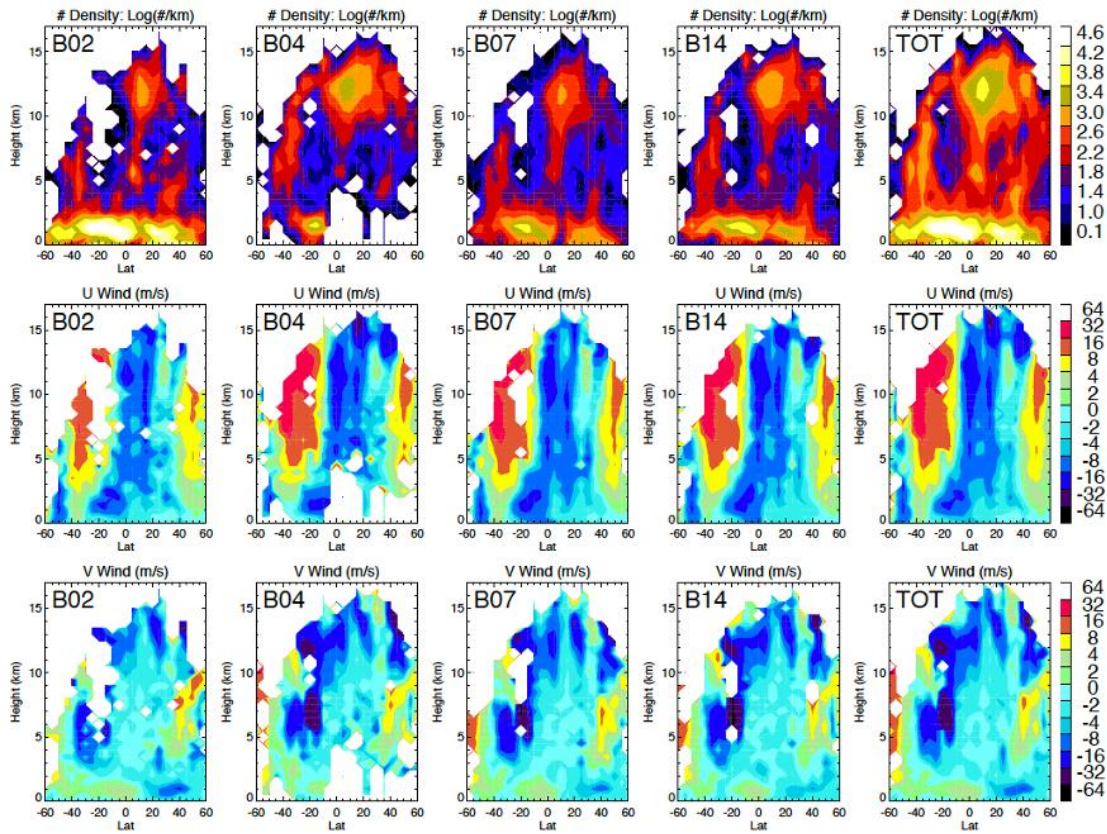
Figure 12. Zonal mean distributions of cloud height, *u*- and *v*-wind retrievals (as in Figure 11) for the four spectral bands as a function of latitude and altitude. The TOT is the averaged zonal mean of the results from four spectral bands for the entire domain of FD-FD retrievals.

3.2.2 Water Vapor Features

The Water Vapor (WV) emissions at thermal IR wavelengths (Bands 8-10) produce brightness temperature gradients that can be tracked for AMV detection [36]. One of the advantages of using WV features is that they help to extend AMV measurements into cloud-free regions. WV features tend to have a larger spatiotemporal correlation length than cloud features in IR or VIS images. Some of the trackable WV features are shown in Figure 13 for B08, which has a radiative-transfer weighting function favoring the upper troposphere. Because of strong WV emission and absorption, low-level cloud features seen by an IR window channel (e.g., B14) are mostly absent in B08. A disadvantage with WV tracking is that there can be cases where winds flow in the direction parallel to the WV gradient [37] and then derived AMVs would not accurately represent winds.

Compared to an IR window channel (e.g., B14), the WV channels from Bands 8 (upper-level), 9 (mid-level) and 10 (lower-level) produce significantly more AMVs in the upper troposphere (Figure 14). As shown in Figure 13, a WV channel can also detect upper-tropospheric cloud features, and therefore the increased number of AMVs is a result of more trackable atmospheric features (clouds and WV gradients) in the upper troposphere from Bands 8-10. Although Band 10 is designed to have a WV weighting function favoring the lower troposphere, the stereo-wind results only show a moderate increase in the AMVs there, most of which are found at the latitudes with a relatively drier upper troposphere.

To further quantify the relative importance of WV features to the total number of AMVs from the IR channels, we compare the AMV yield percentage of B08 (WV + clouds) with B14 (clouds only) for different template sizes (Table 4). Because WV features are characterized by a larger (meso-to-synoptic) spatial scale, we speculate that the yield percentage would increase with the template size used in the stereo-wind pattern matching. Since B08 AMVs contain both cloud and WV features, we use the ratio of the number of B08 AMVs over B14 as an indicator of the WV contribution to the total

562   AMVs. Table 4 compares this ratio for four template sizes from 12x12 to 96x96 pixels in two height
563   ranges (>2 km and >5km). For both height ranges, the ratio shows a consistent increase with template
564   size, confirming the increased contribution of WV AMVs as larger features are tracked in the mid-to-
565   upper troposphere. The analysis shows that additional 60% of AMVs come from WV features at
566   heights > 2 km and 90% at heights > 5 km, if the 48x48 template size is used.

567

568
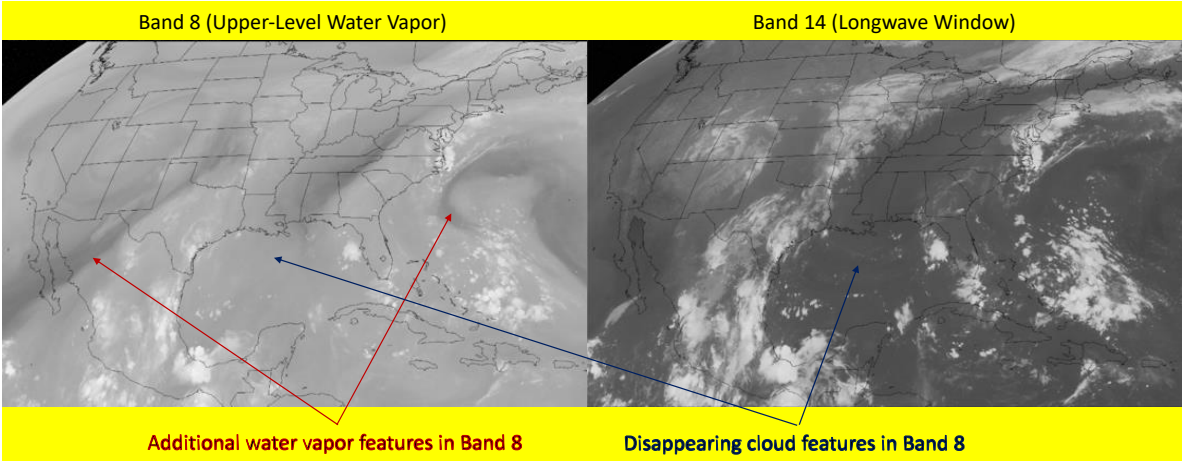
569   **Figure 13**. WV and cloud features as seen B08 and B14 from September 10, 2020 at 12Z. (CONUS
570   image credit: Space Science and Engineering Center at the University of Wisconsin).

571
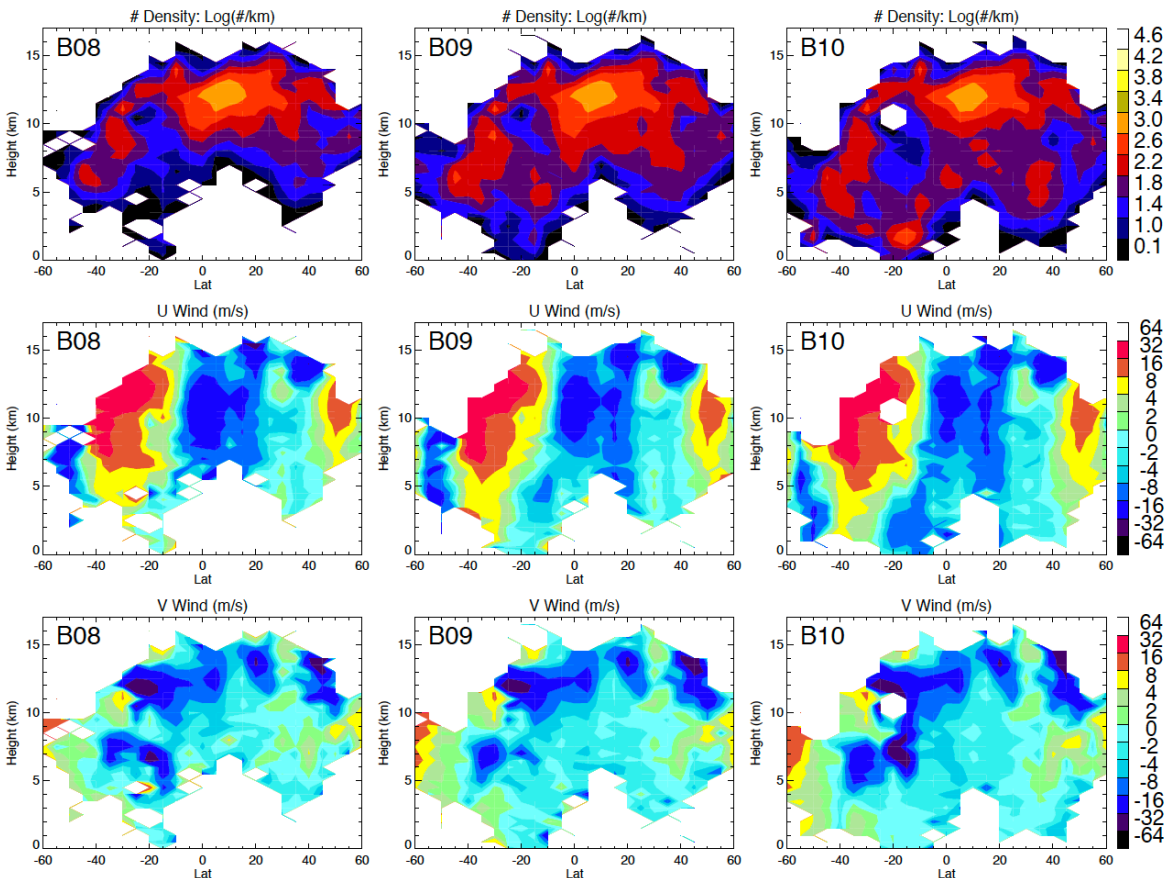
572   **Figure 14.** As in Figure 12 but for WV Bands 8-10. A template size of 24x24 is used for these stereo-
573   wind retrievals.

574   **Table 4.** Yield comparisons of stereo-wind retrievals in the mid- and upper-troposphere

Template Size	Heights > 2km			Heights > 5km		
	Band 8	Band 14	Ratio	Band 8	Band 14	Ratio
12x12	17.7%	13.8%	1.3:1	17.5%	11.3%	1.5:1
24x24	37.4%	26.1%	1.4:1	36.8%	21.1%	1.7:1
48x48	53.6%	33.6%	1.6:1	52.6%	27.5%	1.9:1
96x96	59.6%	39.0%	1.5:1	58.3%	32.2%	1.8:1

575

3.3 Applications

577   The GEO-GEO stereo-wind technique now enables new science investigations of the
578   atmospheric processes that require full diurnal sampling at mesoscale and accurate knowledge of
579   height variations. As shown in this section, fast processes such as deep convective clouds and fire
580   plumes can benefit particularly from the 10-min GEO-GEO refresh with the IR channels, to study the
581   lifecycle of tropical cyclones and wildfire development/transport. In addition, the accurate (~300 m)
582   stereo-wind height retrievals have a great potential for tracking and characterizing planetary
583   boundary layer clouds and their structural evolution. In the following we will illustrate these science
584   applications with the stereo-wind retrievals for Tropical Storm Imelda (2019), Hurricane Hanna
585   (2020), California Creak Fire (2020), and marine stratus/stratocumulus in the Southeastern Pacific.

586   3.3.1 Deep Convection from Tropical Cyclones

587   GEO-GEO stereo imaging has the advantage of tracking deep convective systems continuously
588   and 24-hours per day in the TIR channels. To illustrate the evolution of the deep convective dynamics,
589   we apply the stereo GEO-GEO algorithm to Tropical Storm Imelda (2019) and Hurricane Hanna (2020)
590   on consecutive days during a period just before their respective landfalls. B07 and B14 from CONUS-
591   FD pairs are used for the stereo height and AMV retrievals with a 10-min refresh rate. To process the
592   large GOES-16/17 data set, we developed scripts to parallelize and run the stereo-winds research
593   algorithm seamlessly on NASA's supercomputer Discover. Figure 15 shows the regions of interest
594   where the stereo-wind high-cloud fraction and divergence retrievals for Imelda and Hanna are
595   mapped at the time shortly before landfall. The embedded box indicates the area where the area-
596   average time series are computed. The high-cloud fraction and cloud-top divergence are derived
597   from the stereo-wind 10-min retrievals, whereas the precipitation is extracted from the half-hourly
598   Integrated Multi-satellite Retrievals for GPM (IMERG) data using NASA's Giovanni search tool.
599   Figure 16 shows a strong diurnal variation in the area-averaged high-cloud fraction, divergence,
600   and precipitation during the cyclone's intensified period. Imelda had a short lifetime after its
601   formation in the Gulf of Mexico on Sep. 14 (Day 257). It rapidly developed into a tropical storm before
602   reaching the east coast of Texas on Sep. 17 (Day 260). Imelda weakened substantially after landfall,
603   but it brought large amounts of flooding rain to Texas and Louisiana. As seen in Figure 16. Time
604   series of area-averaged cloud top divergence (black), precipitation (red) and high-cloud fraction (blue)
605   for Imelda (2019) and Hanna (2020). The area-averaged divergences and high-cloud fraction from
606   B07 (left) and B14 (right) are obtained from the measurements with cloud top heights > 10 km in the
607   box area (as indicated in Figure 15). The cloud fraction is divided by 5 to plot on the divergence scale.
608   The divergence value is normalized by the total number of observations available in the domain, to
609   reflect an area mean of divergence strength. (LST=Local Satellite Time, the diurnal cycle of the stereo-
610   wind divergence lags the precipitation cycle by ~6 hours, followed by the high-cloud fraction. While
611   the divergence and high-cloud fraction rise nearly simultaneously at the beginning of a diurnal cycle,
612   the peak of cloud fraction is significantly lagging behind the divergence peak, which is expected as
613   the increase in high-cloud fraction is initiated by the divergence in a convective system.
614   The diurnal cycles of cyclone rainfall and deep convection over tropical oceans are strongly
615   correlated, showing a maximum in the early morning [38,39]. A study with the 10-year hurricane
616   database from GOES IR imagery shows that the diurnal variation of mature cyclones is driven by the
617   convective pulses near the inner core, which starts in the late afternoon and early evening hours and
618   grows into intense deep convective cells in the early morning [40]. These convective pulses, while

619 growing in intensity, move away from the core at night and extend 100's km by the early morning.
620 In the previous study with the high-resolution stereo-wind retrievals, we were able to identify
621 mesoscale divergence flows at the top of Hurricane Michael (2018) [11]. For the peak time of cyclone
622 precipitation, there are significant differences in the diurnal variations between the precipitations in
623 ocean and land environments [41]. The cyclone precipitation over land tends to peak twice: one in
624 early morning and the other in the late afternoon. In the study period shown in Figure 16, both Imelda
625 and Hanna were mostly in an open ocean environment, but the observed lag between the divergence
626 and precipitation warrants further investigation and validation.
627   The comparison for Hurricane Hanna (2020) in Figure 16 is perhaps a case that requires more
628 validation on the precipitation and divergence measurements. Hanna, also a short-lived hurricane,
629 was formed in the central portion of the Gulf of Mexico on July 23 (Day 205). It strengthened to a Cat-
630 1 hurricane and made landfall in Texas on July 25 (Day 207), before dissipating rapidly over Mexico
631 on July 27 (Day 209). Like Imelda, the similar diurnal variations and lags are observed for Hanna in
632 the area-averaged time series for precipitation, divergence and high-cloud fraction. However, on Day
633 208 the divergences from B07 and B14 exhibit some significant differences, while the precipitation
634 shows strong oscillations with a large mean. These large oscillations are not evident in either
635 divergence or high-cloud fraction measurements, suggesting a potential issue with the IMERG data.
636 Furthermore, both the divergence and cloud fraction indicate a reduction in the storm intensity,
637 whereas the precipitation data still implies a high storm strength. Other than Day 208, comparisons
638 during the rest of the period reveal the consistent lagged correlations among precipitation,
639 divergence, and high-cloud fraction, as found for the Imelda case.
640

641

642   **Figure 15.** A snapshot of Tropical Storm Imelda (2019) and Hurricane Hanna (2020) cloud height (left
643   panels) and cloud top (>10 km) divergence (right panels) retrieved from B14. The stereo-wind
644   retrievals are made from the CONUS-FD pairing with 10-min sampling. The box in each case indicates

645   the region of interest for comparison with the domain-average precipitation data. For Imelda, the box
646   area is (110°W-98°W, 32°N-38°N) and for Hanna it is (110°W-100°W, 30°N-35°N).

647

648   **Figure 16.** Time series of area-averaged cloud top divergence (black), precipitation (red) and high-
649   cloud fraction (blue) for Imelda (2019) and Hanna (2020). The area-averaged divergences and high-
650   cloud fraction from B07 (left) and B14 (right) are obtained from the measurements with cloud top
651   heights > 10 km in the box area (as indicated in Figure 15). The cloud fraction is divided by 5 to plot
652   on the divergence scale. The divergence value is normalized by the total number of observations
653   available in the domain, to reflect an area mean of divergence strength. (LST=Local Satellite Time.)

654   3.3.2 Planetary Boundary Layer (PBL)

655   As a shallow (<2 km) layer between the surface and the free atmosphere, the PBL has been a
656   challenge for remote sensing from space, because it requires a good vertical resolution to distinguish
657   the layer from the surface and a horizontal resolution better than mesoscale to resolve its spatial
658   variability. The separation between PBL, surface, and the mid- and upper tropospheric clouds is
659   difficult with radiometric data due to the largely varying lapse rate in atmospheric temperature
660   profiles [42-44]. Here the stereoscopic technique provides a new look to the problem without relying
661   on radiometric calibration and lapse rate assumptions. More importantly, the GEO-GEO stereo
662   imaging can track PBL top variations every 10 min, which is critical for studying PBL cloud lifecycle
663   and transition between different cloud regimes.
664   Cloudy PBLs in the Southeastern Pacific (SEP) provide a good test case for GOES-16 and -17
665   stereo winds, which are expected to resolve the top of stratocumulus-topped boundary layer (STBL)
666   with a relatively good vertical (~300 m) and horizontal (~6 km) resolution in B02. The SEP region is
667   often covered by widespread low-lying stratus clouds that are radiatively important for Earth's
668   climate system because their enhanced albedo can effectively reflect solar radiation and reduce the

669   energy absorbed on Earth [45]. Figure 17 shows GOES-17 B02 radiances for a typical STBL region.
670   Reflectivity and therefore radiance variations span about 3 orders of magnitude due to the presence
671   of broken stratocumulus clouds [46]. Stratocumuli are convective clouds and their vertical
672   development is constrained by the PBL structure [43] and they provide good patterns for stereo
673   tracking. As the STBL deepens above ~1 km, its top starts to decouple from the well-mixed PBL with
674   the surface moisture supply [47], transitioning from overcast stratocumulus (closed cells), to open
675   cells, to trade cumulus clouds.

676   The rising PBL top and transition from stratocumulus to trade cumulus clouds are evident in an
677   example of 3D-Wind stereo height retrievals (Figure 17). On July 25, 2020 (17:20Z) there was a
678   counterclockwise cyclonic circulation in the region that advected the PBL air northeastward from the
679   Peruvian coast (cold SST) to the tropics (warm SST). The PBL dynamics and top height are perhaps
680   better illustrated by the 3D-Wind B02 (visible) than B14 (IR) outputs in which a finer (template size
681   12x12 km and sampling size 6x6 km) horizontal resolution is employed for retrieving the B02 AMV
682   and CTHs. The clear-sky region near the coast has no AMV and CTH retrievals from the stereo-winds
683   method. However, once clouds start to form with a feature distinguishable from featureless ocean
684   surfaces, stereo-winds method can retrieve a shallow layer that appears to be ~300 m above the
685   surface. These CTHs rise to 1.5-2 km along the wind direction with a nearly uniform coverage before
686   the clouds break down to open cells. The observed STBL in the SEP represents the classical transition
687   from stratocumulus to trade cumulus clouds, which further verifies the ~300 m vertical resolution of
688   the 3D-Wind's GEO-GEO technique.

689   One of the most valuable PBL properties that the stereo-winds method can provide is mesoscale
690   divergence (Figure 18). Because of its high-resolution AMV retrievals and layer assignments, it
691   becomes feasible with the GEO-GEO stereo-wind technique to derive the stratocumulus divergence
692   and convergence at mesoscale using neighboring wind measurements at the same height. A similar
693   technique was proposed to derive mesoscale divergence and vertical motions using dropsonde wind
694   profiles in a 100-km domain [48]. As revealed in the divergence map from stereo winds (Figure 18)
695   the observed mesoscale divergence/convergence is small for clouds with CTH < 1.2 km but becomes
696   oscillatory with increasing amplitudes for CTH > 1.2 km. This is the critical height level for the PBL
697   top decoupling. The divergence/convergence oscillations at mesoscale are a result of cloud self-
698   organization from small scales to a larger scale through thermodynamic processes [49] and often
699   manifest themselves in a rosette-like form [50]. Because stratocumulus clouds break down through
700   self-organization and precipitation processes, the mesoscale divergence/convergence is considered
701   as an important indicator of the cloud evolution from closed to open cell transition [51]. The stereo-
702   winds maps show a consistent picture as expected for closed-to-open-cell transition in terms of PBL
703   top variations and divergence increases. The new data set from GEO-GEO stereo imaging, especially
704   with 10-min sampling, will provide great insights and a better understanding of STBL structures,
705   dynamics, and their evolution with different environments.
706
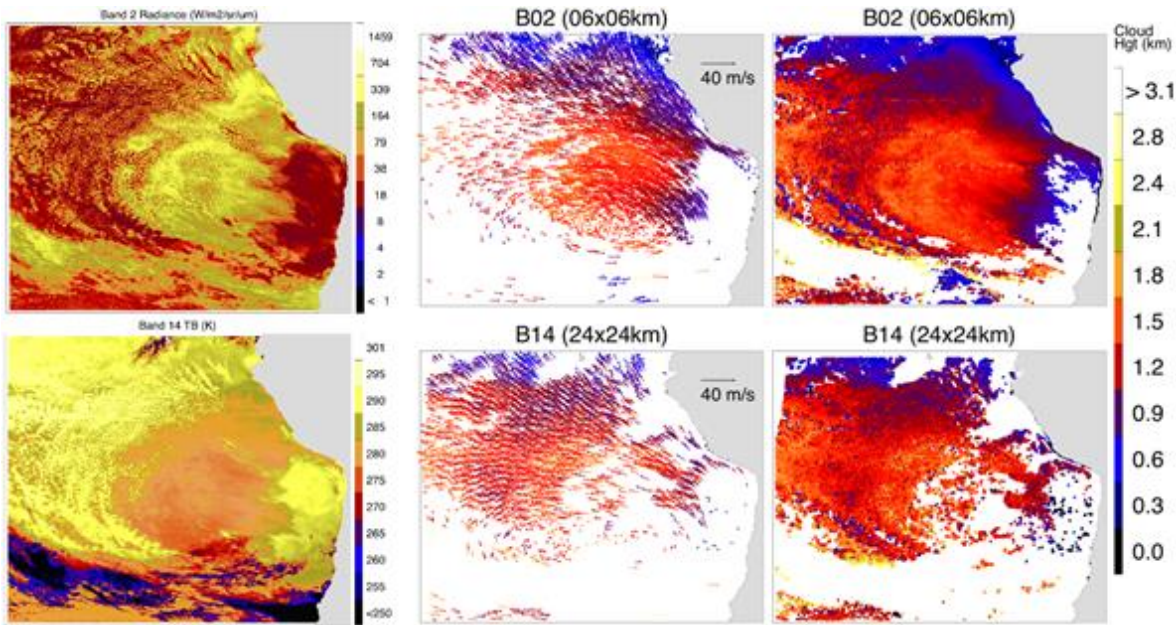
Figure 17. The stereo-wind retrievals from GOES-16 and -17 B02 (top) and B14 (bottom) in the southeastern Pacific (SEP) (110°W-70°W,0-40°S) on 25 July 2020, 17:20Z. For each band, the radiance map, along with AMV and stereo CTH retrievals from are shown. The B02 radiances are in W/m²/sr/μm and B14 in brightness temperature (K). The AMV vectors are color-coded by CTH with sampling resolution indicated in the title of each panel. For illustration purposes, the AMV vectors are thinned by a factor of 64 for B02 and 8 for B14 in the plots.
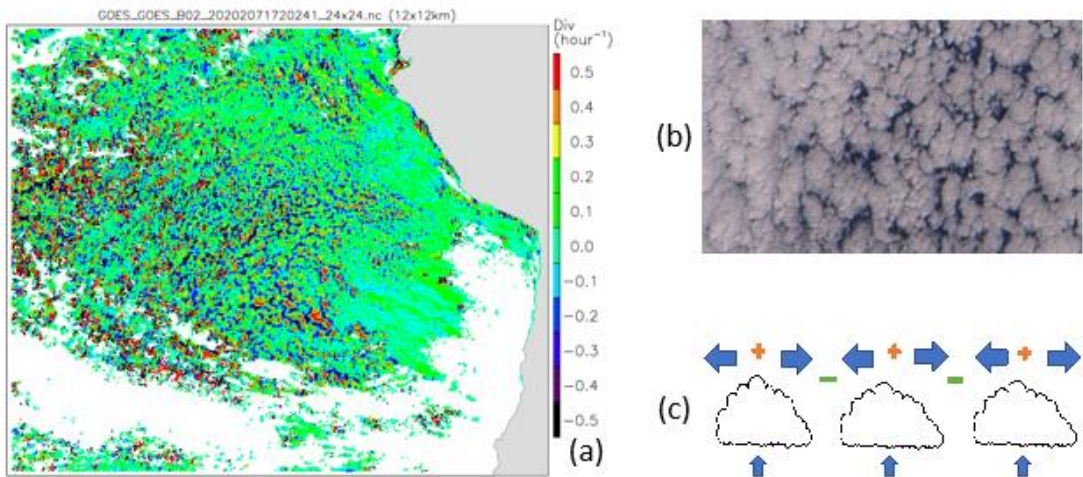
Figure 18. (a) The mesoscale divergence derived from stereo-wind AMV retrievals at CTH < 3 km. The divergence is calculated from the AMVs in a 36x36 km domain but sampled at the 12x12 km grid. An image of closed and open cells of stratocumulus clouds is shown in (b). The divergence and convergence associated with cloud cells are illustrated in (c).

3.3.3 Fire Plumes

The 2020 wildfire season (August-to-November) on the U.S. West Coast is one of the worst in the modern history and the largest to date for California. As of mid-September, five of the top 20 largest wildfires in California history occurred in 2020. Although the fire season is still underway, the California Department of Forestry and Fire Protection reports this year's wildfires through September 23, 2020 have consumed 3.6 million acres as compared to less than 43,500 acres for the

725 same period in 2019 [52]. In early September, an intense heatwave broke temperature records in
726 several locations in California, including 49°C in Los Angeles on September 6. The Hot-Dry-Windy
727 Index (HDW), which is used to determine and manage wildfire risks from adverse atmospheric and
728 surface conditions [53], reached a peak on September 8, while several major broke out in California,
729 Oregon, and Washington.

730   Intense wildfires not only destroy property and habitat, but they also impact public health in a
731 much wider area with plumes shooting above the atmospheric PBL and spreading over radii of
732 hundreds to thousands of kilometers. The GOES-17 images in Figure 19 captured an explosive
733 pyrocumulonimbus (pyroCb) cloud from Californian Creek Fire on September 9. The stereo-wind
734 retrievals show that the plume heights reached 14+ km above the terrain with a wind speed of 15-20
735 m/s (Figure 20). The fire plume quickly spread into a large area within two hours and moved to the
736 south. By September 12, the upper-tropospheric fire plumes generated from the West Coast had been
737 advected thousands of kilometers into the Pacific, the East Coast, and the Atlantic.

738   Fire pyroCbs are rare events and require LEO sensors to observe at the right place at the right
739 time [54]. The rapid refresh with the stereo-wind technique from GOES-16 and -17 not only facilitates
740 capturing more pyroCb events but also tracking their development and structural evolution. Figure
741 21 shows the time evolution of the plumes from Creek Fire. The area-mean divergence and curl
742 indicate pulse forcings at ~15:20Z and 19:00Z, followed by a steady increase in area-mean plume
743 height and wind changes (direction and speed) on that day. The intensive fire forcing at ~15:20Z
744 generated an explosive pyroCb with the area-mean plume height peaking above 10 km in a 30-min
745 period. As the plume height increases, the associated curl decreases (divergence increases slightly),
746 and the plume wind speed increases with direction. Because of the intense and variable heating from
747 wildfires, the fire-atmosphere interaction has been a challenging research topic [55]. The sudden
748 change in the upper-tropospheric wind velocity, coincident with the forcing increase, suggests that a
749 fire behavior change could impact dynamics through fire-atmosphere coupling processes.

750   Plume heights and winds exhibit a strong diurnal cycle in the Creek Fire development (Figure
751 21). Early studies with GOES fire radiative power (FRP) observations showed that the FRP and
752 burned area tend to peak shortly after the local time noon (~13:00) in the west CONUS [56].
753 Depending on fuel consumption and smoke emission rates, accurate characterization of plume
754 diurnal variations plays an important role in estimating biomass burning emissions for air quality
755 prediction. The time series from the stereo-wind retrievals show that the plume height and wind
756 speed from Creek Fire peak at ~16:00 local time over the three intensive burning days (DOY 252-254),
757 approximately 3 hours after the FRP peak. This lag is expected in a sense that the upper-level plume
758 buildup would follow the increase in fire intensity. The pulse at 15:20Z on September 9 reflects an
759 additional forcing from the pyroCb on the top of the anticipated smoke fire diurnal cycle.

760
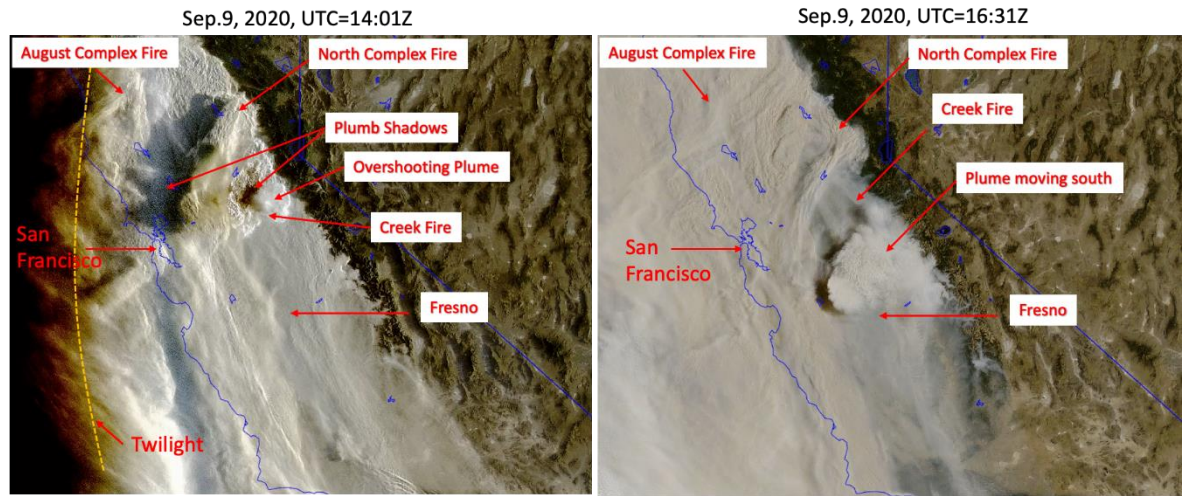
761 **Figure 19.** PyroCb generated from Creek Fire on September 9, 2020 when three major wildfires were
762 burning in the northern California with very poor air quality and visibility in the region. The fire
763 plumes overshot the level of neutral buoyancy and created a visible deep convective core. The plume

764 core's shadows on the plume deck are evident in the early morning hour. The overshooting smoke
765 plumes allow a widespread impact of these wildfires over 1000's kilometers (Image credit: Space
766 Science and Engineering Center at the University of Wisconsin).

767
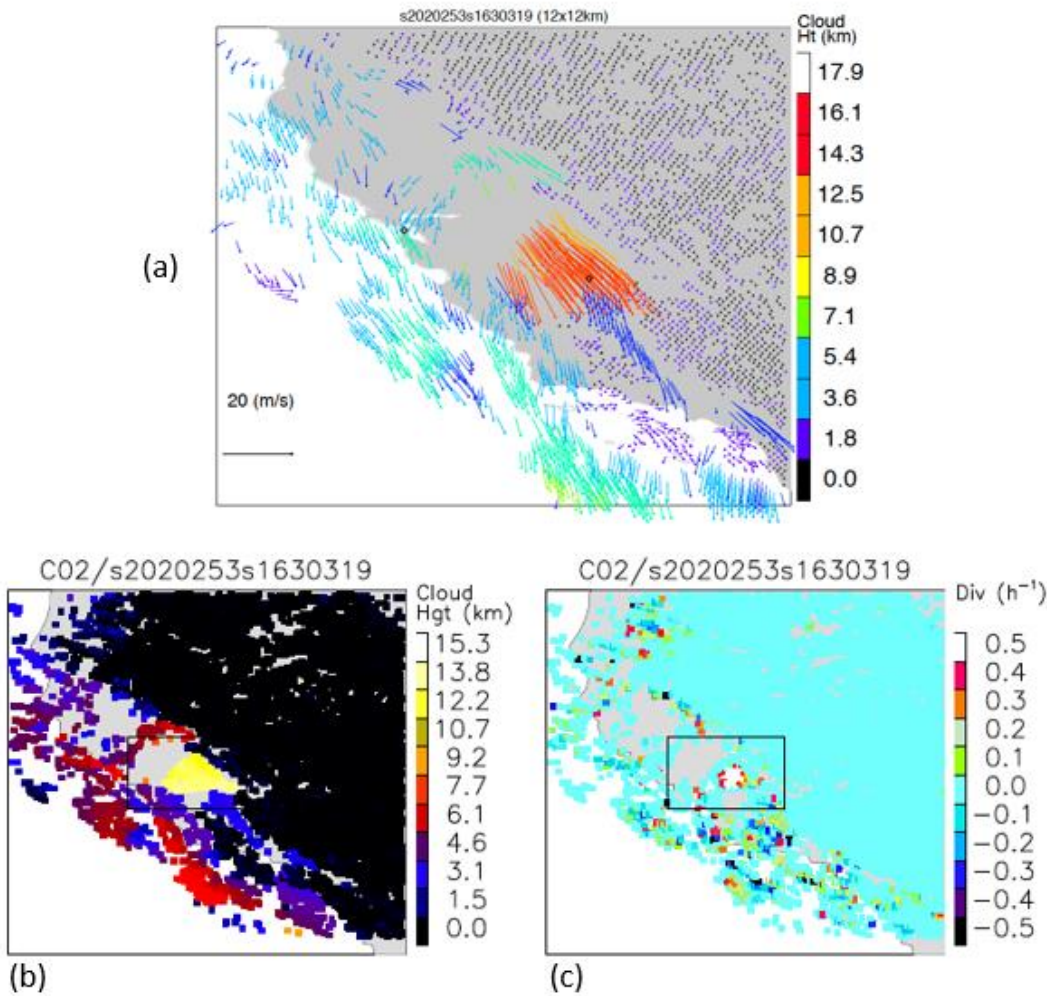
768 **Figure 20.** The B02 stereo-wind retrievals from 16:30Z on September 9 for (a) wind velocity, (b) plume
769 height above terrain, and (c) divergence. The embedded box indicates the area used to monitor the
770 area-mean time series of these variables.

771
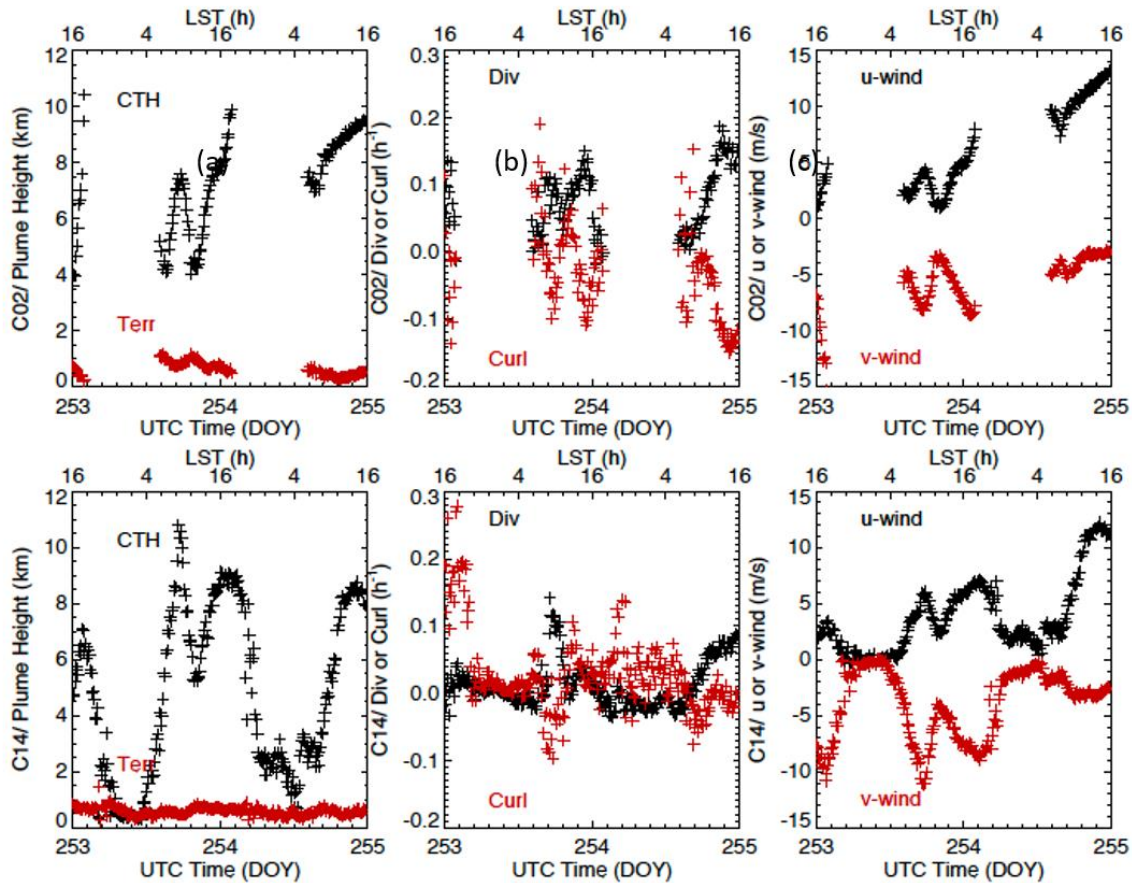
Figure 21. Time series of area-mean (a) plume height (CTH) above terrain, (b) divergence (black) and curl (red), u- (black) and v-wind (red) variations during September 8-12 (DOY 252-256). Area-averaged terrain heights (red) are also included in (a) and vary slightly with time because it is averaged only for the site locations where the quality stereo height is reported.

4. Discussion

In Section 3, we presented results validating the stereo-winds method and demonstrated several application areas where the stereo-wind height assignments will likely be beneficial. Here, we discuss the error characteristics of stereo winds and quantify their sensitivities to INR (geometric) errors, errors in satellite ephemeris, and errors in time assignments. We then discuss the problems of tracking of orographic clouds and comparing satellite winds to rawinsonde observations with prospects for positive NWP impacts.

4.1 Error Analysis

Retrieval accuracy is affected by the quality of the INR, accuracy of knowledge of satellite position vectors, and the accuracy of times assigned to matched site locations. These sensitivities are analyzed below.

4.1.1 INR Errors

Accurate retrieval of wind height using stereo methods from two GEO spacecraft is possible because of accurate INR. The sensitivities of the retrievals to INR errors is most easily understood in the simplest case where we consider a point on the equator at a longitude bisecting the nominal position of each satellite as shown in Figure 22.

792

793
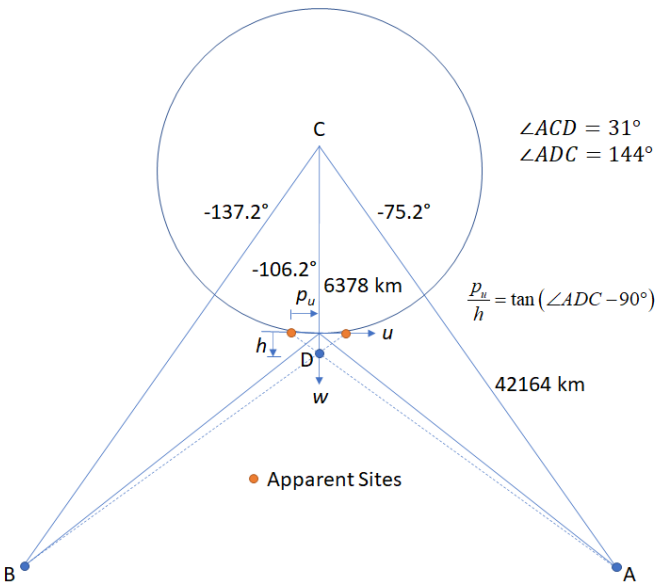
Figure 22. The geometry of stereo-winds retrieval with two GOES spacecraft is represented (not to scale) at a site bisecting the two satellites on the equator. The angle $\angle ACD$ is half the longitude separation between the spacecraft and $\angle ADC$ is found by the law of cosines. In the limit as $h \to 0$, the ratio of the parallax to the height approaches $\tan(\angle ADC - 90°)$.

For the above geometry, each column in Table 5 shows the error in the retrieved state variable, in m or m/s, that is realized from a +1 km displacement in the assigned site for the tracer in each of the five input scenes individually. A triplet of CONUS scenes from GOES-16 and a pair of consecutive FD scenes from GOES-17 are assumed with the first and last members of the triplet (A±) being simultaneous with the FD pair (B±).   Table 5 also presents the objective function value (χ) after the state solution.

Table 5. Sensitivities of individual states are shown to +1 km displacements applied individually to each of the five input scenes at the midpoint between GOES-16 and -17 on the equator.

	East-West (u) +1 km					North-South (v) +1 km				
State	A-	A0	A+	B-	B+	A-	A0	A+	B-	B+
p_u (m)	250	-1000	250	250	250	0	0	0	0	0
p_v (m)	0	0	0	0	0	248	-993	248	248	248
h (m)	-343	0	-343	343	343	0	0	0	0	0
V_u (m/s)	-0.83	0	0.83	-0.83	0.83	0	0	0	0	0
V_v (m/s)	0	0	0	0	0	-0.83	0	0.83	-0.83	0.83
χ (m)	500	0	500	500	500	702	0	702	702	702

The five state rows by ten displacement columns above form a matrix H that gives the response of the retrieval process in the linear approximation to small displacements in units of each state component per km of displacement.   The following linear combinations of displacements D provide interpretations ($H \cdot D$) as pure motion or pure parallax:

$D = [-1, 0, 1, -1, 1, 0, 0, 0, 0, 0]^T$ km, results in $H \cdot D$ with only nonzero state $V_u = 3.33$ m/s,

$D = [\,0, 0, 0, 0, 0, -1, 0, 1, -1, 1]^T$ km, results in $H \cdot D$ with only nonzero state $V_v = 3.33$ m/s,

$D = [\,0, 0, 0, 1, 1, 0, 0, 0, 0, 0]^T$ km, results in only $p_u = 500$ m and $h = 685$ m being nonzero.

816   The above conforms with expectations, as the ratio of the parallax correction to height 500:686
817   matches the tangent calculation in Figure 22 and a 1 km displacement over 5 minutes is a velocity of
818   3.33 m/s.   Although χ does not combine linearly, it can be calculated for each combination above
819   and is found to be zero in these cases, meaning that their representation as states is exact in terms of
820   the model.   It is also the case that $\chi = 0$ for displacements of A0 in either direction as indicated by
821   the A0 column in Table 5.   This is simply a reflection of the fact that the disparities are measured
822   with respect to the A0 scene and therefore this case is equivalent to displacing all the other scenes in
823   the opposite direction.   The response of the retrieval process is to adjust the site location to
824   compensate and leave the height and wind velocity states unaffected.
825   In addition to the 5-state retrievals, the retrieval process also produces a 5x5 covariance matrix
826   to represent the uncertainties (and their correlations) in the retrieved states.   Assuming that the 1 km
827   displacements for A± and B± are instead independent normally distributed random numbers with
828   means zero and standard deviations equal to 1 km along both axes, the covariance matrix is found to
829   be nearly diagonal in the geometry of Figure 22 and the square root of its diagonal elements are the
830   one-sigma standard errors (or uncertainties): $\sigma(p_u) = \sigma(p_v) = 500\ m$, $\sigma(h) = 685\ m$, and $\sigma(V_u) =$
831   $\sigma(V_v) = 1.67\ m/s$.   We validate these theoretically calculated uncertainties using a Monte Carlo
832   simulation with 10^5 trails representing random errors in measured u- and v-displacements with
833   respect to A0 and running the retrieval model to find: $\sigma(p_u) = 499\ m$, $\sigma(p_v) = 496\ m$, $\sigma(h) = 684\ m$,
834   $\sigma(V_u) = 1.67\ m/s$, and $\sigma(V_v) = 1.65\ m/s$.   Hence, if we can represent the statistics of the disparity
835   measurements in terms of their uncertainties, we can have an estimate of the uncertainties of retrieved
836   states.   This is particularly useful in the LEO-GEO geometry, even if real disparities are likely to have
837   more complicated statistics, with biases and correlations, to diagnose when stereo winds fail because
838   the lines of sight from the two satellites are nearly parallel.   The covariance matrix possesses a
839   divergent eigenvalue in such cases.   This pathology does not occur in the GEO-GEO geometry
840   except when the longitude separation of the satellites approaches zero when retrievals fail essentially
841   everywhere.
842   The relevant INR metrics for the GOES-R system are Navigation (NAV) error and Frame-to-
843   Frame Registration (FFR) error, interpreted as angles in the fixed grid.   NAV error represents the
844   offset between the ABI imagery and a reference map or nearly perfectly geo-registered imagery from
845   another source.   FFR represents the stability of NAV between consecutive frames.   The GOES-R
846   specification is 28 μrad for NAV, 21 μrad for FFR (resolution < 2 km), and 28 μrad for FFR (resolution
847   = 2 km).   Each number represents the absolute value of the mean error plus three times the standard
848   error.   Measured performance on orbit is considerably better [57].   Our INR error model parameters
849   provide a simple description of the INR errors that envelope the demonstrated on-orbit performance
850   of both satellites.   For ABI B02, there can be a small negative bias of about 2 μrad in NAV in the EW
851   direction, and an about 5 μrad (3σ) random NAV error in both axes.   The B02 FFR errors are unbiased
852   and have about 5 μrad (3σ) random error in both axes.   Typical NAV performance for the 2 km IR
853   channels (e.g., B07) are measured at 16 μrad (3σ) in both axes and FFR at about 8 μrad (3σ) in both
854   axes.   We represent these INR errors in a Monte Carlo analysis by modeling the navigation errors
855   for the A and B sequences such that the error statistics of individual scenes match the NAV
856   parameters and the statistics of the differences between successive scenes match the FFR parameters.
857   The conversion between distance on the ground and fixed-grid angle at the SSP is 1 km equals 28
858   μrad and increasing away from the SSP.   In the geometry of Figure 22, a 28 μrad angular
859   displacement is elongated in the u-direction by $K_u = 1/\cos(180° - \angle ADC) = 1.24$ but not in the v-
860   directions (i.e., $K_v = 1$) and is the same for both satellites.   We apply these factors to derive the site
861   location errors from the INR errors for our Monte Carlo analysis.
862   Figure 23 shows the retrieval error statistics from the Monte Carlo simulation with 10^5 trials and
863   using the INR performance parameters for the 0.5-km ABI B02 and the 2-km ABI B07 channel.   The
864   bias has been represented only in the A satellite to avoid cancellation.   It introduces a small bias in
865   the height retrievals.   The error statistics shown are smaller than those observed from the ground-
866   point retrievals (Figures 7 and 8), but there are other error sources that should be included.   Mapping
867   error would represent any geometric error introduced in the process of remapping the B± scenes into

868   the fixed grid of satellite A.   It could include topographic, shading, or shadowing effects.   With a
869   moving target, the mapping error may be uncorrelated between B± but be correlated for a stationary
870   feature.   There is also matching error that would represent the uncertainty in locating the matching
871   place of templates from A0 in in A± and B±.   Matching error may depend on the template sizes.

872
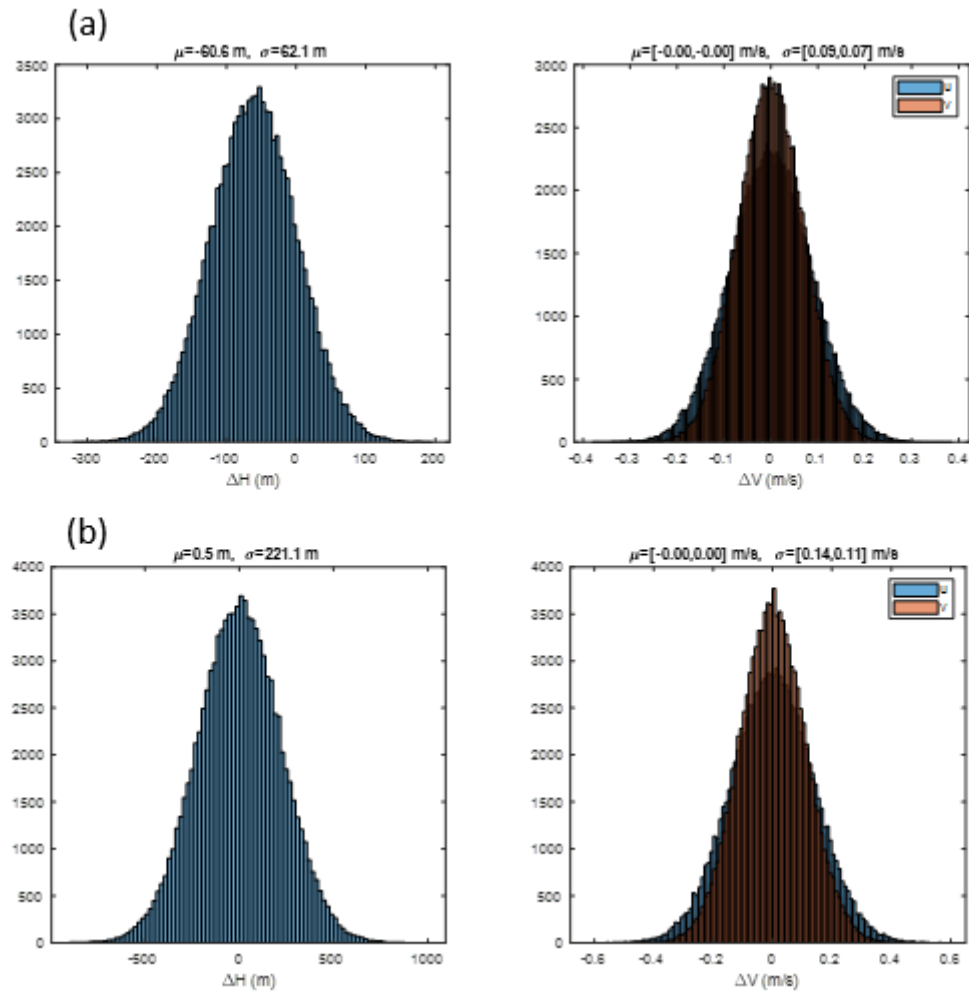
873   **Figure 23.** Monte Carlo simulation results show the retrieval errors statistics with demonstrated on-orbit
874   GOES-R INR performance for (a) ABI B02 and (b) ABI B07.   Mean and standard errors are listed in order
875   of the [u, v]-directions.

876   FFR errors can be observed in the disparity measurements of ground points.   Figure 24 shows
877   the measured disparities between A± and A0 within the class of ground points.   The restriction to
878   the A satellite removes parallax and remapping from consideration and the restriction to ground
879   points assures that the measurements are being made on stationary objects.   Here, we can observe a
880   sudden jump in the FFR at swath boundaries.   The jump is the signature of another INR error type
881   called Swath-to-Swath Registration (SSR) error.   In this example, the SSR error is ~0.1 B02 pixels in
882   the worst case.   The FFR variation shown within a swath is typically < 0.1 pixel from the mean.
883   These results also confirm our ability to track objects with subpixel resolution and to be sensitive to
884   motion on the order of 0.1 pixels or better.
885
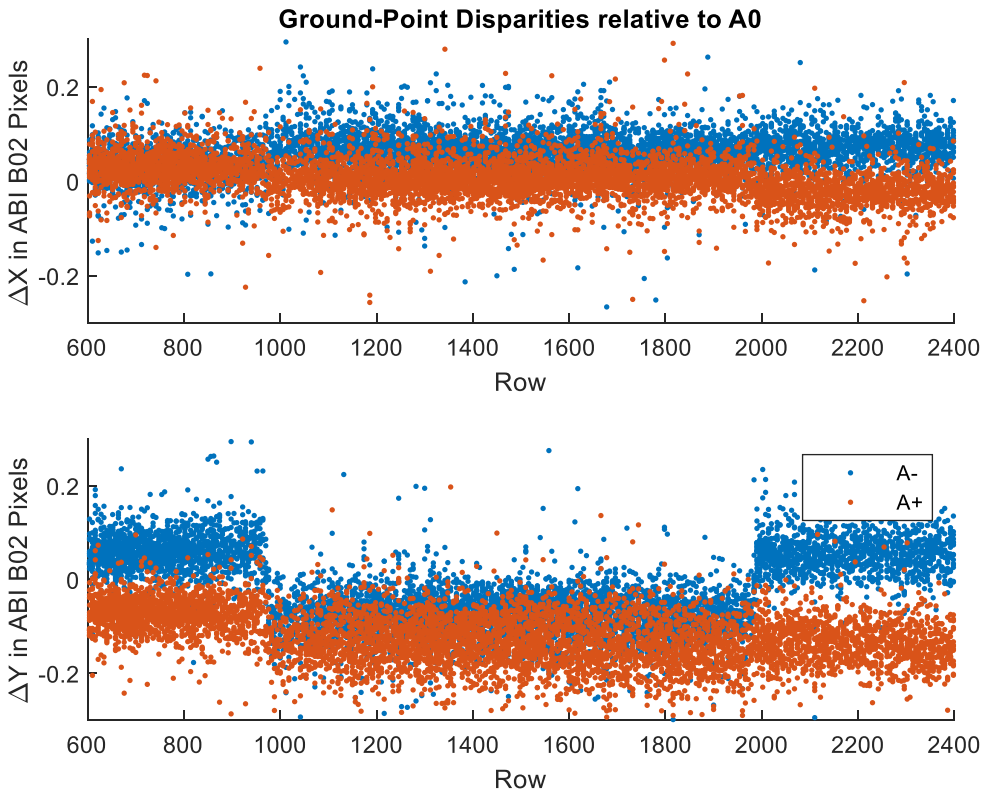
Figure 24. Observed FFR error as a function of CONUS scene row number shows a jump in SSR at swath boundaries. The A0 scene is a B02 CONUS image from GOES-16 at 2020/207 17:16.

Himawari INR errors have been characterized as part of an effort to post-process the Himawari Standard Data (HSD) Level-1 product for land applications [58]. This characterization shows biases in NAV with mean values that can vary systematically with the hour of the day up to at least July 2019. Similar results have been published by [59]. We use the HSD products in our work but can apply an a priori compensation for the AHI navigation based on such a characterization when available. Uncompensated biases can be as large as one 0.5-km pixel. Figure 25 shows the height bias from an EW NAV bias equal to one 0.5-km pixel applied to the AHI imagery. The retrieved height bias scales in proportion with the EW NAV bias. A NS NAV bias has almost no effect.
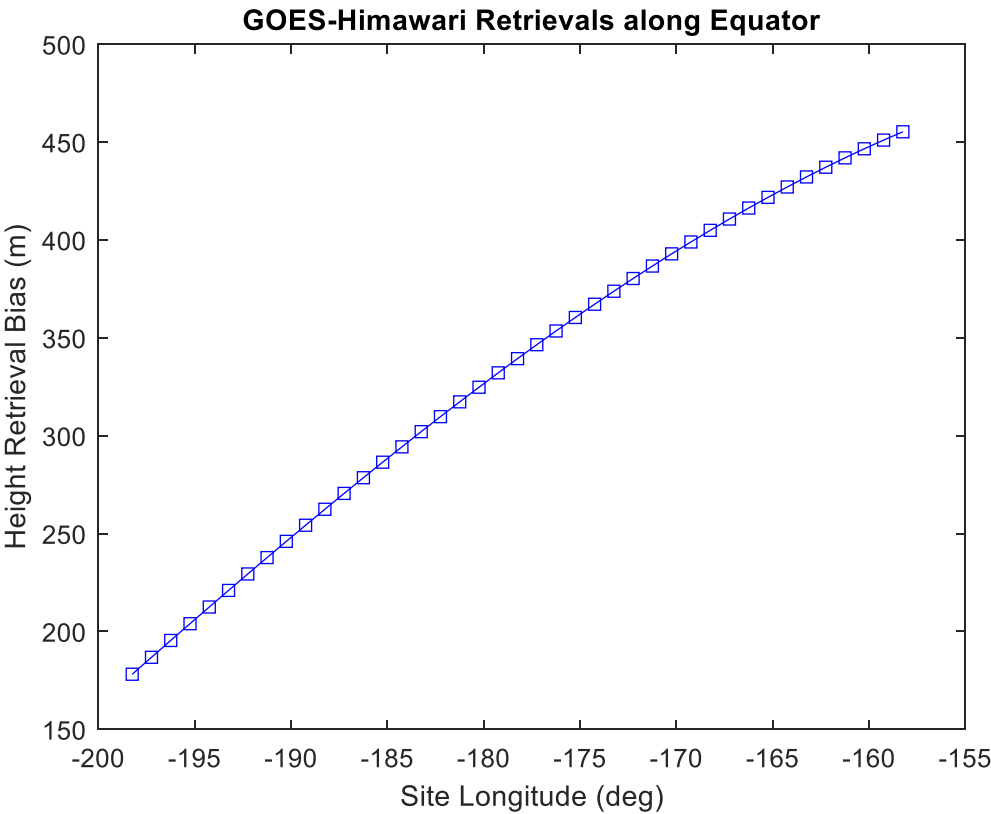
Figure 25. Retrieved height bias grows with the distance from the Himawari-8 SSP along with the elongation of AHI pixels on the ellipsoid.   The height bias will grow in proportion with the EW NAV bias, which is a single 0.5-km pixel in this case.

Clearly, it is advantageous that large INR errors should be compensated when they can be compensated.   The overlap in coverage between GOES-17 and Himawari-8 is almost all over water, so height biases for ground points are not easily accessed.   However, landmarks over Australia and Asia, which are outside of the overlap could be used to identify NAV biases in individual AHI scenes or a priori models used.

4.1.2 Ephemeris Errors

The ephemerides of the A and B satellites are used in the retrieval algorithm.   Ephemeris errors mostly affect the height retrievals.   Here, we consider the case where an error is introduced in the GOES-17 ephemeris and the Himawari-8 ephemeris is left as is.   Specifically, GOES-17 is assumed to be positioned at 137.0°W rather than 137.2°W for the purposes of exercising the retrieval algorithm, while leaving the definition of the GOES-17 fixed-grid reference longitude as 137.0°W.   This changes the calculated baseline between the satellites.   Figure 26 shows retrieved height differences for collocated retrievals in the two cases plotted versus retrieved height in site longitude bands.   The height errors are in proportion to the height with a slope that grows as the site moves away from the GOES-17 SSP and toward Himawari-8.   The slope of a regression in each longitude band would be proportional to the ephemeris error.   Since a real ephemeris error will be much smaller than 0.2°, the induced retrieval errors should be much less than 100 m.

918
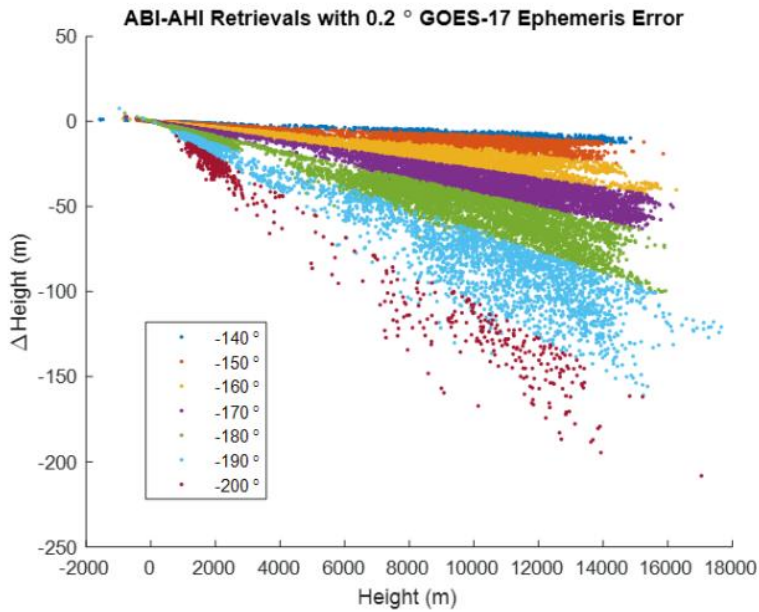
919   **Figure 26.** Retrieved height differences are proportional to the wind height with a constant of
920   proportionality that varies with the site longitude. The errors become more significant as the site
921   moves away from GOES-17 and toward Himawari-8.

922   4.1.3 Time-Assignment Errors

923   Time assignments for the matches of each template against each scene affect both the wind speed
924   and its height assignment. Considering GOES-16 and -17, we introduce a +10 s time bias for all sites
925   in the B+ scene and examine the errors introduced in the retrievals by comparing them against the
926   retrievals without errors. Figure 27 shows that the time bias affects the retrieved wind speed in
927   proportion to the speed. The height assignments are also affected, but in a slightly more complicated
928   way related to the wind component parallel to the baseline between the satellites (i.e., approximately
929   the u-component of wind velocity). This is expected since the retrieved wind velocity is derived
930   from perceived horizontal motion divided by lapsed time and the horizontal position is corrected for
931   non-simultaneity using the time tags in the retrieval model that would in turn affect the parallax for
932   a simultaneous observation.

933
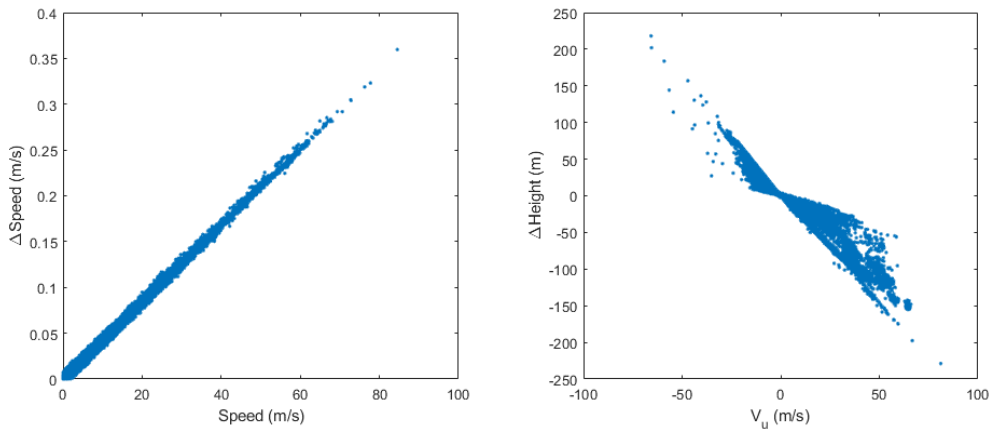
934   **Figure 27.** Retrieved wind speeds and heights are affected by the presence of a +10 s time assignment
935   error in the B+ scene roughly in proportion to the speed. The graphs plot the differences between
936   retrievals with and without the time bias applied to the B+ scene.

937 The impact of a time-tag error would be roughly linear with its magnitude and errors on the
938 order of 30 seconds could happen when a site is mis-assigned to a scan swath. Were this to occur
939 over a background of moving clouds, there would be an apparent discontinuity in the retrieval fields
940 as the swath boundary is crossed.

941 *4.2 Orographic Cloud Effects*

942 Caution is required to use the AMVs derived from orographic clouds. Although the stereo-wind
943 heights associated with the orographic clouds may be accurate, the AMVs from orographic clouds
944 may not reflect the true air flow over the top of mountains. Orographic clouds are forced by the
945 topography and appear as standing-wave clouds with a height close to the terrain. Typically, they
946 are anchored along the mountain ridges or around inhomogeneous terrains. As a result, the AMVs
947 from orographic clouds are close to zero, manifesting themselves as a slow bias in wind speed if they
948 are not identified.

949 We can evaluate the effects of near-surface orographic clouds, possibly for the first time over a
950 continental scale, because of the highly accurate stereo-wind height and AMV retrievals offered by
951 stereo methods. As shown in Figure 28, orographic clouds tend to develop in the afternoon hours
952 over the southwest U.S. after heating of the land surface creates conditions favorable for their
953 formation. In other words, a strong diurnal cycle is expected for orographic cloud effects. To quantify
954 the orographic cloud effect, we compare the terrain height with the stereo-wind B02 height retrievals
955 that have a low (<1 m/s) wind speed for all daytime hours. As more orographic clouds appear in a
956 region, the area-mean height bias against terrain will increase. Such effect is seen in Figure 29 where
957 the height bias over the southwest U.S. increases with local time over the course of daytime
958 orographic cloud development.

959 Over a larger domain (e.g., the U.S. and Central America), orographic clouds manifest
960 themselves as a high bias in the stereo-wind terrain height (Figure 30. (a) Stereo-wind terrain height
961 retrieval from the B02 CONUS-FD stereo; and (b) Stereo-wind bias from the true terrain height. The
962 stereo-wind heights with wind speed < 1 m/s are averaged to a 0.5°×0.5° longitude-latitude grid from
963 all daytime hours on July 26, 2019), with "terrain height" defined as the height with wind speed < 1
964 m/s; therefore, it reports the tops of orographic clouds if they are present. In Figure 30, we find that
965 orographic clouds can reach as high as ~1.5 km over the mountains in Mexico or Central America,
966 which is much higher than those over the Rocky Mountains. Orographic uplift is one of the major
967 cloud formation mechanics, among convectional lifting, convergence/frontal lifting and radiative
968 cooling processes. Atmospheric moisture convergence at the ridge–valley scale help to trigger valley
969 convection and produce orographic clouds and subsequent precipitation [60]. Frequent, persistent
970 orographic cloud cover is critical for tropical montane cloud forests [61]. A more reliable detection of
971 orographic clouds and their variability with the stereo-wind algorithm can better characterize spatial
972 patterns of cloud immersion over cloud-forest areas.
973
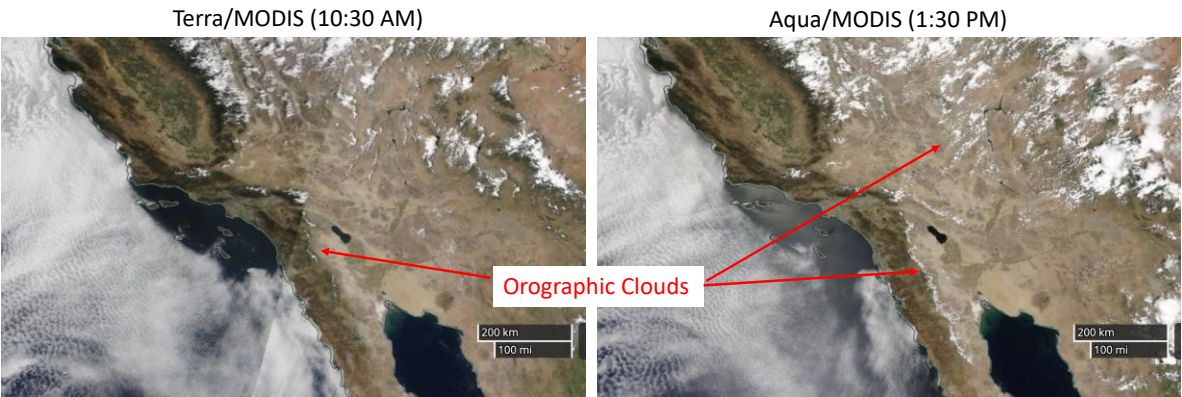
975 **Figure 28.** Orographic cloud development seen by MODIS between morning and afternoon on July
976 26, 2019 over California, Arizona, and Mexico.

977
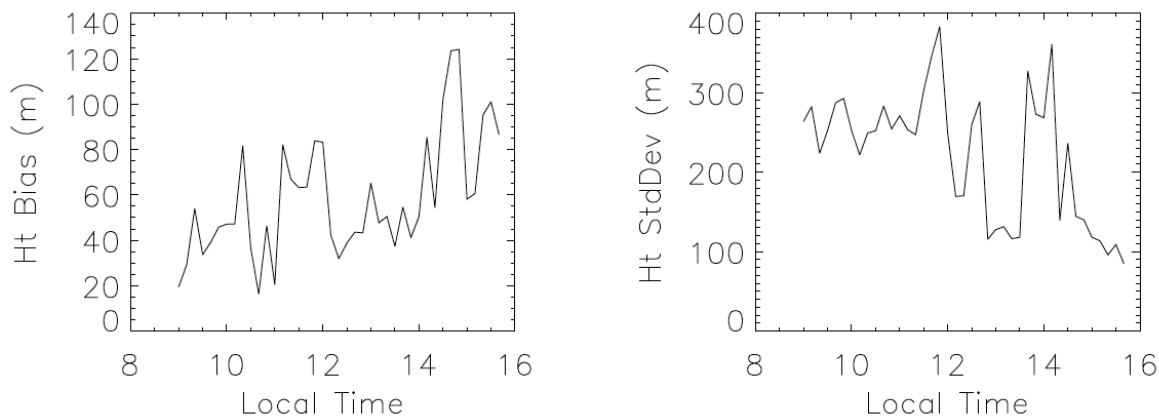
978   **Figure 29.** Local time dependence of the terrain height bias (left) and its standard deviation (right) in
979   the southwest U.S. (111°W-105°W, 32°N-38°N) from the 3D-wind Band 2 retrievals for July 26, 2019.

980
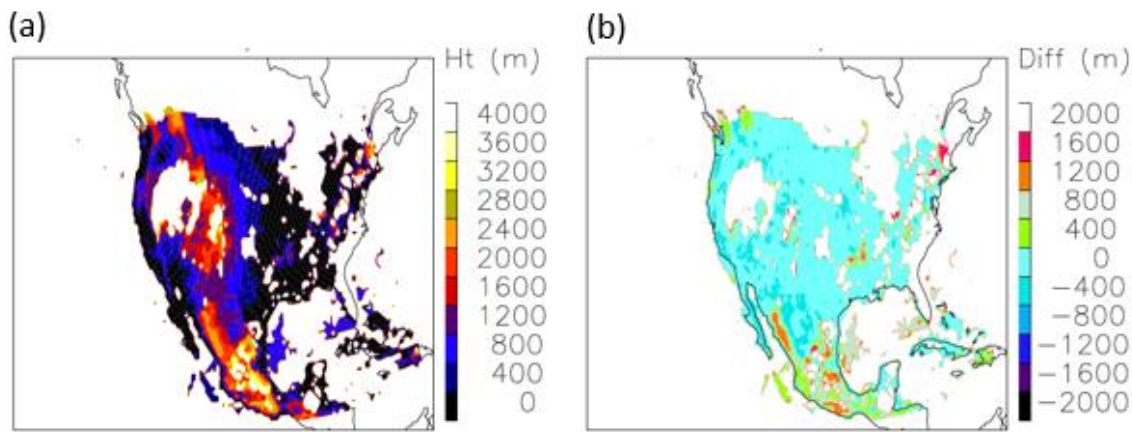
981   **Figure 30.** (a) Stereo-wind terrain height retrieval from the B02 CONUS-FD stereo; and (b) Stereo-
982   wind bias from the true terrain height. The stereo-wind heights with wind speed < 1 m/s are averaged
983   to a 0.5°x0.5° longitude-latitude grid from all daytime hours on July 26, 2019

984   *4.3 Rawinsonde Comparisons and NWP Implications*

985   Satellite-derived winds are routinely evaluated against spatially and temporally collocated
986   rawinsonde observations to assess their quality [7,8,28,62-64]. While this is the general practice, it is
987   important to understand that the differences in the winds obtained from these observing systems
988   come from a combination of observing system measurement errors, representativeness errors, and
989   atmospheric spatial/temporal variability (e.g., wind shear, vertical moisture distribution). Wind
990   representativeness errors are the result of differences in what these two observing system's
991   measurements represent.   Radiosonde wind measurements are essentially point or line samples
992   along a slant path through the atmosphere, whereas satellite winds are representative of motion that
993   over an atmospheric volume. As a result, the range of typical error variances between satellite winds
994   and rawinsondes winds range from 1.5-7.5 m/s [65].
995   While the ground-point statistics cited in Table 2 and the theoretical arguments in Section 4.1
996   indicate that the velocity retrieval errors should be much smaller than Cordoba [65], we should keep
997   in mind that ground points differ from cloud targets in many respects, including a static morphology,
998   opaqueness, non-acceleration, zero velocity shear, and (except in mountains) confined to a thin layer
999   or surface.   Therefore, we would expect ground-point statistics to exaggerate the accuracy of the
1000   retrievals in terms of their representing physical winds.   Supposing that representativeness errors
1001   are larger than the underlying accuracy indicated by the ground points and theoretical considerations,

1002   it would not be surprising that even significant improvements in satellite wind measurements will
1003   have a small numerical impact on the MVD metric. Yet, such improvements may have significant
1004   impact on NWP. One of the largest sources of errors for satellite winds is the height assignment
1005   [4,66-67]. Velden and Bedka [68] have estimated that height assignment is the dominant factor in
1006   satellite wind uncertainty and contributes up to 70% of the total error. A reliable estimate of the
1007   magnitude of the height-assignment error is critical for NWP data assimilation and must be
1008   accounted for [69]. Numerous studies have also been done to investigate the interpretation and
1009   impact of interpreting satellite winds as a layer-average wind [64,68,70-71]. The stereo method
1010   enables the retrieval of very accurate cloud heights, and therefore, very accurate satellite wind height
1011   assignments; and therefore, we expect potential for the stereo winds to contribute to improving the
1012   skill of NWP forecasts.

5. Conclusions

1013
1014   The stereo-winds method jointly solves for AMVs and their heights in the atmosphere using
1015   feature tracking to measure disparities between a reference scene and its multi-temporal repetitions
1016   and at least one view from a different vantage point. An important feature of our approach is that
1017   it does not require synchronization between observing systems, only the ability to assign times to
1018   pixels. In previous works [10,11], the stereo-winds method was developed for LEO-GEO
1019   combinations. Its application to GEO-GEO combinations is fully developed in the present work.
1020   Our collaboration has developed two codes and applied them to combinations including GOES-16, -
1021   17, and Himawari-8.
1022   AMV height assignment is an important problem considering that typical wind speeds increase
1023   significantly with increasing height (decreasing pressure level). Operational satellite wind products
1024   rely on AMV height assignments that use IR methods regardless of whether features are being
1025   tracked in an IR or VIS channel. Such methods rely on differential absorption from cloud-top to
1026   space or modeled temperature versus height (pressure) profiles [1-8]. The latter can be susceptible
1027   to error, particularly in the presence of inversions or stratospheric folding. Stereo methods offer a
1028   direct method of height assignment that can be used as an alternative or complementary method
1029   where there is overlapping GEO-GEO or LEO-GEO coverage. Stereo methods can be applied to any
1030   pairing of similar spectral channels. We have exhibited several application areas where stereo
1031   methods provide insight into atmospheric processes, including deep convection in tropical cyclones,
1032   processes in the PBL, and the dynamics of wildfire smoke plumes. Ultimately, we expect its greatest
1033   impact to be in the field of numerical weather prediction. In future work, we anticipate continuing
1034   the development of prototype products and testing their impact on forecast skill as part of a path
1035   towards operationalizing stereo winds at NOAA. A stereo capability will be particularly useful
1036   when working with GOES-17, which shares overlaps with both GOES-16 and Himawari-8. The
1037   GOES-17 LHP anomaly [15,16] causes IR channels used for operational height assignments to become
1038   nonfunctional at certain times of day near the equinoxes which impacts the coverage and quality of
1039   AMVs. Stereo methods provide a means to make accurate AMV height assignments under these
1040   conditions to mitigate the impact of the anomaly.
1041   Stereo methods are effective thanks to the improved INR performance (i.e., geometric accuracy
1042   and stability) offered by systems such as GOES-R and will work well with other systems in the GEO
1043   ring offering similar performance. We analyzed the sensitivity of stereo-wind retrievals in the
1044   presence of INR and other errors to demonstrate that expected retrieval errors are in family with the
1045   observed retrieval errors from our validations against fixed ground targets.
1046   The improved quality of the stereo winds is due to their improved height assignments. Our
1047   validations against rawinsonde observations generally demonstrate superior performance from
1048   stereo winds, which is an indication that stereo winds have good potential for improving forecasting
1049   skill. The addition of the stereo winds to the suite of NOAA's operational winds can be expected to
1050   increase the utilization of NOAA's satellite winds at NOAA and international partner operational
1051   NWP forecast systems with the potential for measurable improvements in the accuracy of global and
1052   regional weather forecasts.

1053   We intend in future work to extend our validation of stereo winds to include comparisons with
1054   Aeolus, additional rawinsonde datasets, and collocated aircraft winds.   We also plan to engage with
1055   NWP centers to stimulate interest in conducting an OSE.

1056   **Supplementary Materials:** The following are available online at www.mdpi.com/xxx/s1, ABI time-model LUTs.

1057   **Author Contributions:** Conceptualization, James L. Carr, Dong L. Wu and Jaime Daniels; Data curation, Mariel
1058   D Friberg and Wayne Bresky; Formal analysis, James L. Carr; Funding acquisition, Dong L. Wu and Jaime
1059   Daniels; Investigation, James L. Carr, Dong L. Wu and Jaime Daniels; Methodology, James L. Carr, Dong L. Wu,
1060   Jaime Daniels and Wayne Bresky; Project administration, Dong L. Wu and Jaime Daniels; Resources, Dong L.
1061   Wu and Jaime Daniels; Software, James L. Carr, Mariel D Friberg, Wayne Bresky and Houria Madani;
1062   Supervision, Dong L. Wu and Jaime Daniels; Validation, James L. Carr, Dong L. Wu, Jaime Daniels and Wayne
1063   Bresky; Visualization, James L. Carr and Wayne Bresky; Writing – original draft, James L. Carr, Dong L. Wu,
1064   Jaime Daniels and Wayne Bresky; Writing – review & editing, James L. Carr, Dong L. Wu, Jaime Daniels, Mariel
1065   D Friberg, Wayne Bresky and Houria Madani.

1066   **Funding:** Carr Astronautics received support from NASA Goddard Space Flight Center under the
1067   NNG17HP01C contract through Support for Atmospheres, Modeling, and Data Assimilation (SAMDA).   Carr
1068   Astronautics and IMSG received support form NOAA/STAR and the GOES-R Program. Mariel D. Friberg's
1069   research was supported by the NASA Postdoctoral Program at the NASA Goddard Space Flight Center and
1070   administered by Universities Space Research Association. Resources supporting this work were provided by the
1071   NASA High-End Computing (HEC) Program (NASA program manager: Tsengdar Lee) through the NASA
1072   Center for Climate Simulation (NCCS) at Goddard Space Flight Center. Additional supports were provided by
1073   Terra/MISR (NASA program manager: Hal Maring), Decadal Survey Incubation Study Teams: Planetary
1074   Boundary Layer (NASA program manager: Gail Skofronick-Jackson).   The APC was funded by NASA.

1075   **Acknowledgments:** Special thanks to Stacey Williamson at Carr Astronautics who assisted with the manuscript.

1076   **Conflicts of Interest:** The authors declare no conflict of interest.

Appendix A

1078   The ABI Level-1 product is constructed so that 0.5-km pixels nest within 1-km pixels that in turn
1079   nest within 2-km pixels.   The Swath Transition Line (STL) separates pixels that are resampled from
1080   detector samples belonging to one ABI swath from those resampled from next swath of detector
1081   samples.   Pixels are never resampled from a mix of two swaths.   The STL is always drawn on the
1082   boundary of a 2-km pixel and is the same for all spectral bands.   There are 22 swaths in an ABI FD
1083   and 21 STLs separating them.   The STL governs the choice of which candidate pixel is selected for
1084   the Level-1 product in the overlap between swaths; therefore, knowledge of the STL is required to
1085   ascertain which pixels belong to which swaths to model pixel times.   The STL is not visible to users
1086   of the ABI Level-1 product, so it must be modeled.   This can be done well, but not perfectly.
1087   Figure A1 shows the STL from a test conducted for a patch to the Data Operations (DO) software
1088   in the GOES-R Core Ground System where the ABI Level-1 product is constructed.   The Level-1
1089   product is created and distributed in "release regions" shown as magenta blocks and released one by
1090   one in the GOES Rebroadcast (GRB) data stream.   The GRB data stream is recovered at a second
1091   location where the blocks are assembled into a rectangular canvas to populate the Level-1 netCDF
1092   product files.   Individual swaths are commanded to begin and end at the same fixed grid addresses
1093   every FD and small adjustments are made onboard so as to efficiently cover the scene using swaths
1094   that have only a small overlap between them.   The centerline of this overlap nominally bisects the
1095   midpoint between consecutive scan trajectories (green lines).   This would be a good guess for the
1096   STL; however, the STL algorithm actually places the STL (red and blue points) slightly above the
1097   overlap midline in this test.   The behavior of the STL can be complicated as the scan moves off the
1098   Earth; however, we only care about the STL for Earth pixels.   The STLs that are interior to the Earth
1099   are represented as blue points.   Their behavior is such that the STL is nominally about a dozen 2-km
1100   pixels to the north of the overlap bisection line but can fluctuate up or down along the width of the
1101   swath.   Figure A2 provides a histogram of the bias in the STL relative to the overlap bisection line
1102   observed over the FD.   One can more practically assume that the STL is always drawn with the same
1103   bias (12 IR pixels north) since the fluctuations from the nominal cannot be predicted.   The bias value

1104 is approximately half the height of the tallest overlap across all the spectral bands.   It is possible that
1105 the bias value could depend on the DO release, but the STL cannot deviate too far from the overlap
1106 midline.   The behaviors of the STLs for the CONUS and MESO scenes are similar in this test.
1107
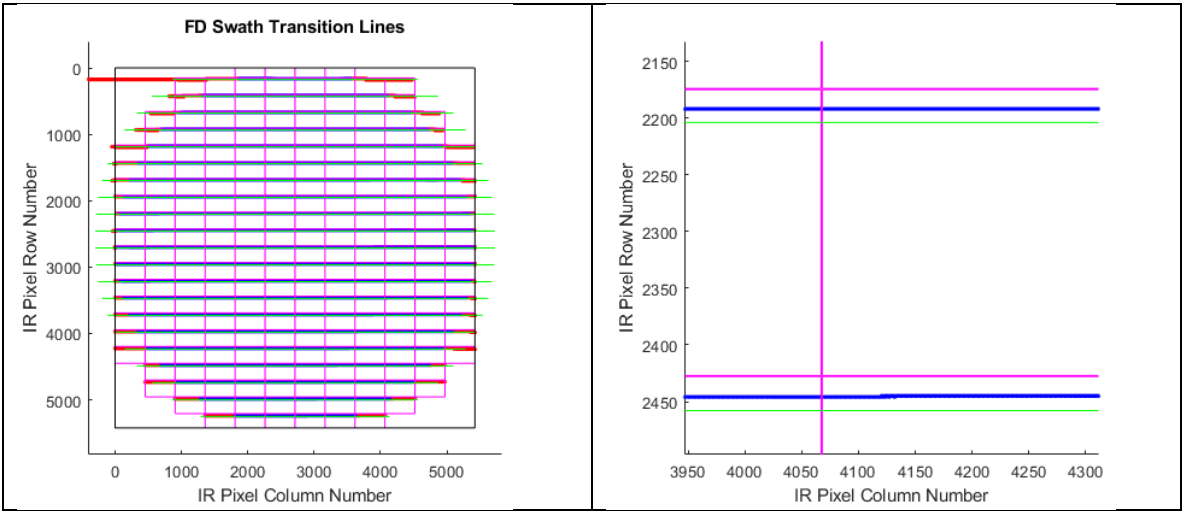
1108   **Figure A1.** The STL interior to the Earth is represented by blue dots and the overlap bisections are
1109   drawn in green.   The complete FD is shown to the left with a zoom to the right.

1110
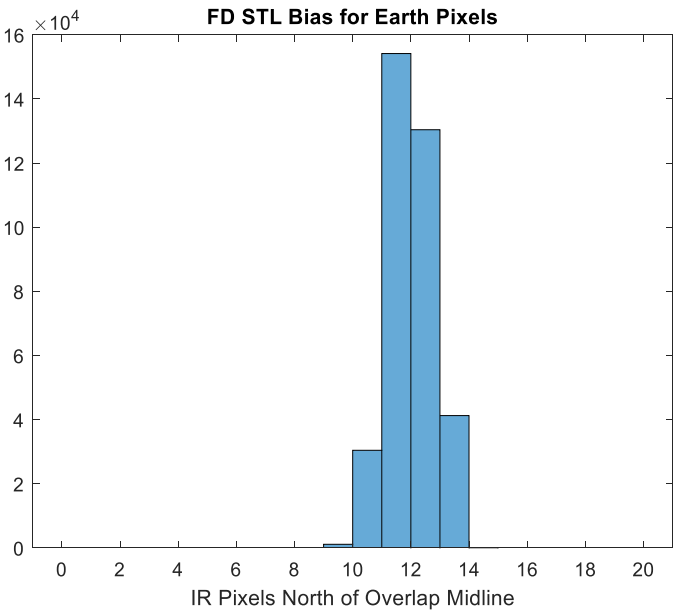
1111   **Figure A2.** Histogram of the bias of the STL with respect to the overlap bisection line for a FD has a
1112   median value of 11 and a mean of 11.5 2-km IR pixels.

1113   The LUTS are constructed for each timeline from the output of a tool called MISTiC that is used
1114 to construct new timelines.   We read a MISTiC html output file to gather the swath start and stop
1115 times and assign the center time for each swath accordingly.   The scan rate of 1.4°/s is used to
1116 calculate the variation in time as the scan progresses from west to east.   STLs are drawn with
1117 constant bias from the overlap bisection lines and the LUT times are offset so that the first pixel in the
1118 first release region has a time stamp equal to zero.   Product times of all channels denote the time of
1119 the first Band 2 detector sample used to construct the Band 2 scene; therefore, the product time is a
1120 good approximation to add to the LUT times to get an absolute time stamp for all pixels within a
1121 Band 2 scene.   However, the detectors for each ABI channel are offset along the scan from each other,
1122 so a small adjustment can be made for each spectral channel using Table A1 below.   The value in

1123 Table A1 for a spectral band minus that of Band 2 should be added to the pixel times as a small final
1124 adjustment.

1125   **Table A1.** Time offsets of the ABI spectral bands relative to the optical center.

Band	1	2	3	4	5	6	7	8
seconds	0.179	-0.055	0.402	0.642	-0.359	-0.642	0.535	0.267
Band	9	10	11	12	13	14	15	16
seconds	0.000	-0.267	-0.535	-0.542	0.551	0.319	-0.256	0.579

1126
1127 Generally, pixel times should be very accurate (~1 s) when we properly assign them to their
1128 swaths.   However, the fluctuations in the STL from its nominal bias is unpredictable.   When a pixel
1129 swath has been mis-assigned then the timing error will be ~30 s for ABI Modes 3 and 6 and somewhat
1130 less for Mode 4.
1131 The LUTs are stored in netCDF files named after the MISTiC html file from which they were
1132 created.   There is a time model variable for each scene in the timeline.   In the case of a timeline with
1133 multiple repetitions of a CONUS, there will be a separate variable for each repetition.   This allows
1134 for there to be differences in the relative relationship between CONUS swaths between scene
1135 repetitions, which happens in some timeline definitions.   The user must know the timeline in use
1136 and the phasing of $t = 0$ in the timeline definition with respect to the top of the hour to relate a
1137 CONUS product file with its repetition in the timeline.   Generally, it can be assumed that the top of
1138 the hour starts a timeline.   There are multiple MESO scenes within all timelines (excerpt for Mode 4,
1139 which has none); however, in all timeline definitions so far, the second MESO swath always follows
1140 the first with the same cadence.   Hence, no distinction between MESO repetitions is made in the time
1141 model.   However, note that some timelines have irregularities in the MESO product times between
1142 repetitions.   These are fully visible with the product time encoded in the file.

1143 **References**

1144 1. Menzel, W.P.; Smith, W.L.; Stewart, T.R. Improved Cloud Motion Wind Vector and Altitude Assignment
1145   Using VAS. *Journal of Climate and Applied Meteorology* **1983**, *22*, 377-384, doi:10.1175/1520-
1146   0450(1983)022<0377:ICMWVA>2.0.CO;2 %J Journal of Climate and Applied Meteorology.
1147 2. Szejwach, G. Determination of Semi-Transparent Cirrus Cloud Temperature from Infrared Radiances:
1148   Application to METEOSAT. *Journal of Applied Meteorology (1962-1982)* **1982**, *21*, 384-393.
1149 3. Schmetz, J.; Holmlund, K.; Hoffman, J.; Strauss, B.; Mason, B.; Gaertner, V.; Koch, A.; Van De Berg, L.
1150   Operational Cloud-Motion Winds from Meteosat Infrared Images. Journal of Applied Meteorology **1993**,
1151   32, 1206-1225, doi:10.1175/1520-0450(1993)032<1206:OCMWFM>2.0.CO;2.
1152 4. Nieman, S.J.; Schmetz, J.; Menzel, W.P. A Comparison of Several Techniques to Assign Heights to Cloud
1153   Tracers. *Journal of Applied Meteorology* **1993**, *32*, 1559-1568, doi:10.1175/1520-
1154   0450(1993)032<1559:ACOSTT>2.0.CO;2 %J Journal of Applied Meteorology.
1155 5. Frey, R.A.; Baum, B.A.; Menzel,W.P.; Ackerman, S.A.; Moeller, C.C.; Spinhirne, J.D. A comparison of cloud
1156   top heights computed from airborne lidar and MAS radiance data using CO2 slicing. J. Geophys. Res.
1157   Atmos. **1999**, 104, 24547–24555.
1158 6. Heidinger, A.K.; Pavolonis, M.J. Gazing at Cirrus Clouds for 25 Years through a Split Window. Part I:
1159   Methodology. *Journal of Applied Meteorology and Climatology* **2009**, *48*, 1100-1116,
1160   doi:10.1175/2008JAMC1882.1 %J Journal of Applied Meteorology and Climatology.
1161 7. Borde, R.; Doutriaux-Boucher, M.; Dew, G.; Carranza, M. A Direct Link between Feature Tracking and
1162   Height Assignment of Operational EUMETSAT Atmospheric Motion Vectors. *Journal of Atmospheric and
1163   Oceanic Technology* **2014**, *31*, 33-46, doi:10.1175/JTECH-D-13-00126.1.
1164 8. Bresky, W.C.; Daniels, J.M.; Bailey, A.A.; Wanzong, S.T. New Methods toward Minimizing the Slow Speed
1165   Bias Associated with Atmospheric Motion Vectors. Journal of Applied Meteorology and Climatology 2012,
1166   51, 2137-2151, doi:10.1175/JAMC-D-11-0234.1.
1167 9. Hasler, A.F. Stereographic Observations from Geosynchronous Satellites: An Important New Tool for the
1168   Atmospheric Sciences. *Bulletin of the American Meteorological Society* **1981**, *62*, 194-212, doi:10.1175/1520-
1169   0477(1981)062<0194:SOFGSA>2.0.CO;2 %J Bulletin of the American Meteorological Society.

1170   10.   Carr, J. L.; Wu, D. L.; Kelly, M. A.; Gong, J. MISR-GOES 3D Winds: Implications for Future LEO-GEO and
1171   LEO-LEO Winds. *Remote Sens.* **2018**, *10*, 1885.
1172   11.   Carr, J.L.; Wu, D.L.; Wolfe, R.E.; Madani, H.; Lin, G.G.; Tan, B. Joint 3D-Wind Retrievals with
1173   Stereoscopic Views from MODIS and GOES. *Remote Sens.* **2019**, *11*, 2100.
1174   12.   Lee, J.; Shin, D.-B.; Chung, C.-Y.; Kim, J. A Cloud Top-Height Retrieval Algorithm Using Simultaneous
1175   Observations from the Himawari-8 and FY-2E Satellites. *Remote Sens.* **2020**, *12*, 1953.
1176   13.   Dehnavi, S.; Maghsoudi, Y.; Zakšek, K.; Valadan Zoej, M.J.; Seckmeyer, G.; Skripachev, V. Cloud Detection
1177   Based on High Resolution Stereo Pairs of the Geostationary Meteosat Images. *Remote Sens.* **2020**, *12*, 371.
1178   14.   Merucci, L.; Zakšek, K.; Carboni, E.; Corradini, S. Stereoscopic Estimation of Volcanic Ash Cloud-Top
1179   Height from Two Geostationary Satellites. *Remote Sens.* **2016**, *8*, 206.
1180   15.   Lindsey, Dan; Griffin, V.; Schrab, K. and Sulliva, P. The GOES-17 Advanced Baseline Imager Anomaly
1181   Mission Recovery. Joint AMS EUMETSAT Satellite Conference **2019**, Boston, MA.
1182   16.   NOAA-NESDIS, 2018: "GOES-17 Loop Heat Pipe Fact Sheet" (PDF). NOAA NESDIS **2018**. Available online:
1183   https://www.nesdis.noaa.gov/sites/default/files/asset/document/NESDIS_factsheet_loopheatpipe.pdf (last
1184   accessed 22 September 2020).
1185   17.   Schmit, T.J.; Gunshor, M.M.; Menzel, W.P.; Gurka, J.J.; Li, J.; Bachmeier, A.S. Introducing the Next-
1186   Generation Advanced Baseline Imager On GOES-R. *Bulletin of the American Meteorological Society* **2005**, *86*,
1187   1079-1096, doi:10.1175/BAMS-86-8-1079 %J Bulletin of the American Meteorological Society.
1188   18.   Schmit, T.J.; Griffith, P.; Gunshor, M.M.; Daniels, J.M.; Goodman, S.J.; Lebair, W.J. A Closer Look at the
1189   ABI on the GOES-R Series. *Bulletin of the American Meteorological Society* **2017**, *98*, 681-698,
1190   doi:10.1175/BAMS-D-15-00230.1 %J Bulletin of the American Meteorological Society.
1191   19.   Bessho, K.; Date, K.; Hayashi, M.; Ikeda, A.; Imai, T.; Inoue, H.; Kumagai, Y.; Miyakawa, T.; Murata, H.;
1192   Ohno, T., et al. An Introduction to Himawari-8/9; Japan's New-Generation Geostationary Meteorological
1193   Satellites **2016**, *94*, 151-183, doi:10.2151/jmsj.2016-009.
1194   20.   GOES- R SERIES PRODUCT DEFINITION AND USERS' GUIDE (PUG) **2018**, 1.2. https://www.goes-
1195   r.gov/users/docs/PUG-main-vol1.pdf (last accessed 22 September 2020).
1196   21.   Coordination Group for Meteorological Satellites (CGMS). LRIT/HRIT Global Specification **1999**,
1197   https://www.cgms-info.org/documents/pdf_cgms_03.pdf (last accessed 22 September 2020).
1198   22.   Yannig, D.; Pascal, H.; Mark, W.; Mounir, L.; Semen, G.; Donny, A.; Paul, B.; Bruno, N.; Jean-Louis, C.;
1199   Olivier, P., et al. The flexible combined imager onboard MTG: from design to calibration. In Proceedings of
1200   Proc. SPIE 9639, Sensors, Systems, and Next-Generation Satellites XIX, 963903
1201   **2015**, https://doi.org/10.1117/12.2196644.
1202   23.   Borde, R.; Carranza, M.; Hautecoeur, O.; Barbieux, K. Winds of Change for Future Operational AMV at
1203   EUMETSAT. *Remote Sens.* **2019**, *11*, 2111.
1204   24.   Alexander, Ken; King, T.; Wolf W. Software Requirements for Supporting Research-to-Operations at
1205   NOAA and Their Implementation in the New SAPF 2.0. **2019,** Joint AMS EUMETSAT Satellite Conference
1206   - September 28 - October 04, 2019, Boston, MA.
1207   25.   Carr, J.L. Georegistration of meteorological images. In Image Registration for Remote Sensing; Le Moigne,
1208   J., Netanyahu, N.S., Eastman, R.D., Eds.; Cambridge University Press: Cambridge, UK, **2011**, 339–354.
1209   26.   Himawari-8/9 Himawari Standard Data User's Guide **2015**, 1.2,
1210   https://www.data.jma.go.jp/mscweb/en/himawari89/space_segment/hsd_sample/HS_D_users_guide_en_v
1211   12.pdf. (last accessed 22 September 2020).
1212   27.   Schmetz, J.; Borde, R.; Holmlund, K.; König, M. Upper tropospheric divergence in tropical convective
1213   systems from Meteosat-8. **2005**, *32*, doi:10.1029/2005gl024371.
1214   28.   Velden, C.; Daniels, J.; Stettner, D.; Santek, D.; Key, J.; Dunion, J.; Holmlund, K.; Dengel, G.; Bresky, W.;
1215   Menzel, P. Recent Innovations in Deriving Tropospheric Winds from Meteorological Satellites. *Bulletin of
1216   the American Meteorological Society* **2005**, *86*, 205-224, doi:10.1175/BAMS-86-2-205 %J Bulletin of the
1217   American Meteorological Society.
1218   29.   Moroney, C.; Horvath, A.; Davies, R. Use of stereo-matching to coregister multiangle data from MISR. *IEEE
1219   Transactions on Geoscience and Remote Sensing* **2002**, *40*, 1541-1546, doi:10.1109/TGRS.2002.801146.
1220   30.   Lonitz, K.; Horváth, Á. Comparison of MISR and Meteosat-9 cloud-motion vectors **2011**, *116*,
1221   doi:10.1029/2011jd016047.
1222   31.   Menzel, W.P. Report from the working group on verification statistics. Proceedings of the Third
1223   International Winds Workshop **1996**, Ascona, Switzerland.

32. Heidinger, A.K. NOAA Enterprise Algorithm Theoretical Basis Document for Cloud Height, Version 3.0, **2015**, 59. Available online: https://www.star.nesdis.noaa.gov/jpss/documents/ATBD/ATBD_EPS_Cloud_ACHA_v3.0.pdf (last accessed 22 September 2020).

33. Wu, D.L.; Ackerman, S.A.; Davies, R.; Diner, D.J.; Garay, M.J.; Kahn, B.H.; Maddux, B.C.; Moroney, C.M.; Stephens, G.L.; Veefkind, J.P., et al. Vertical distributions and relationships of cloud occurrence frequency as observed by MISR, AIRS, MODIS, OMI, CALIPSO, and CloudSat **2009**, *36*, doi:10.1029/2009gl037464.

34. Baker, N. L., P. M. Pauley, R. H. Langland, K. Mueller, K., and Wu, D., An assessment of the impact of the assimilation of NASA TERRA MISR atmospheric motion vectors on the NRL global atmospheric prediction system. Second Symp. On the Joint Center for Satellite Data Assimilation, Atlanta, GA, Amer. Meteor. Soc., **2014**, J3.1, https://ams.confex.com/ams/94Annual/webprogram/Paper231106.html (last accessed 22 September 2020).

35. Mueller, K.J.; Liu, J.; McCarty, W.; Gelaro, R. An Adjoint-Based Forecast Impact from Assimilating MISR Winds into the GEOS-5 Data Assimilation and Forecasting System. *Monthly Weather Review* **2017**, *145*, 4937-4947, doi:10.1175/MWR-D-17-0047.1.

36. Velden, C.S.; Hayden, C.M.; Nieman, S.J.W.; Paul Menzel, W.; Wanzong, S.; Goerss, J.S. Upper-Tropospheric Winds Derived from Geostationary Satellite Water Vapor Observations. *Bulletin of the American Meteorological Society* **1997**, *78*, 173-196, doi:10.1175/1520-0477(1997)078<0173:UTWDFG>2.0.CO;2 %J Bulletin of the American Meteorological Society.

37. Posselt, D.J.; Wu, L.; Mueller, K.; Huang, L.; Irion, F.W.; Brown, S.; Su, H.; Santek, D.; Velden, C.S. Quantitative Assessment of State-Dependent Atmospheric Motion Vector Uncertainties. *Journal of Applied Meteorology and Climatology* **2019**, *58*, 2479-2495, doi:10.1175/JAMC-D-19-0166.1.

38. Nesbitt, S.W.; Zipser, E.J. The Diurnal Cycle of Rainfall and Convective Intensity according to Three Years of TRMM Measurements. *Journal of Climate* **2003**, *16*, 1456-1475, doi:10.1175/1520-0442(2003)016<1456:TDCORA>2.0.CO;2.

39. Bowman, K.P.; Collier, J.C.; North, G.R.; Wu, Q.; Ha, E.; Hardin, J. Diurnal cycle of tropical precipitation in Tropical Rainfall Measuring Mission (TRMM) satellite and ocean buoy rain gauge data **2005**, *110*, doi:10.1029/2005jd005763.

40. Dunion, J.P.; Thorncroft, C.D.; Velden, C.S. The Tropical Cyclone Diurnal Cycle of Mature Hurricanes. *Monthly Weather Review* **2014**, *142*, 3900-3919, doi:10.1175/MWR-D-13-00191.1 %J Monthly Weather Review.

41. Jiang, H.; Liu, C.; Zipser, E.J. A TRMM-Based Tropical Cyclone Cloud and Precipitation Feature Database. *Journal of Applied Meteorology and Climatology* **2011**, *50*, 1255-1274, doi:10.1175/2011JAMC2662.1.

42. Wylie, D.P.; Santek, D.; Starr, D.O.C. Cloud-Top Heights from GOES-8 and GOES-9 Stereoscopic Imagery. *Journal of Applied Meteorology* **1998**, *37*, 405-413, doi:10.1175/1520-0450(1998)037<0405:CTHFGA>2.0.CO;2.

43. Wood, R.; Bretherton, C.S. Boundary Layer Depth, Entrainment, and Decoupling in the Cloud-Capped Subtropical and Tropical Marine Boundary Layer. *Journal of Climate* **2004**, *17*, 3576-3588, doi:10.1175/1520-0442(2004)017<3576:BLDEAD>2.0.CO;2.

44. Wu, D., Hu, Y., McCormick, M. P., Xu, K. M., Liu, Z., Smith, Jr., B., Omar, A. H., and Chang, F. L. "Deriving Marine-Boundary-Layer Lapse Rate from Collocated CALIPSO, MODIS, and AMSR-E Data to Study Global Low-Cloud Height Statistics." IEEE Geoscience and Remote Sensing Letters, vol. 5, no. 4, **2008**.

45. Klein, S.A.; Hartmann, D.L. The Seasonal Cycle of Low Stratiform Clouds. *Journal of Climate* **1993**, *6*, 1587-1606, doi:10.1175/1520-0442(1993)006<1587:TSCOLS>2.0.CO;2.

46. Coakley, J.A. Reflectivities of uniform and broken layered clouds. **1991**, *43*, 420-433, doi:10.1034/j.1600-0889.1991.t01-3-00008.x.

47. Bretherton, C.S.; Wyant, M.C. Moisture Transport, Lower-Tropospheric Stability, and Decoupling of Cloud-Topped Boundary Layers. *Journal of the Atmospheric Sciences* **1997**, *54*, 148-167, doi:10.1175/1520-0469(1997)054<0148:MTLTSA>2.0.CO;2.

48. Bony, S.; Stevens, B. Measuring Area-Averaged Vertical Motions with Dropsondes. *Journal of the Atmospheric Sciences* **2019**, *76*, 767-783, doi:10.1175/JAS-D-18-0141.1.

49. Savic-Jovcic, V.; Stevens, B. The Structure and Mesoscale Organization of Precipitating Stratocumulus. *Journal of the Atmospheric Sciences* **2008**, *65*, 1587-1605, doi:10.1175/2007JAS2456.1.

50. Garay, M.J.; Davies, R.; Averill, C.; Westphal, J.A. ACTINOFORM CLOUDS: Overlooked Examples of Cloud Self-Organization at the Mesoscale. *Bulletin of the American Meteorological Society* **2004**, *85*, 1585-1594, doi:10.1175/BAMS-85-10-1585.

51. Feingold, G.; Koren, I.; Wang, H.; Xue, H.; Brewer, W.A. Precipitation-generated oscillations in open cellular cloud fields. *Nature* **2010**, *466*, 849-852, doi:10.1038/nature09314.

52. Cal Fire, Daily Wildfire Update; Stats and Events. **2020**. https://www.fire.ca.gov/daily-wildfire-report/ (reported on 20 September 2020); https://www.fire.ca.gov/stats-events/ (last accessed 23 September 2020).

53. Srock, A.F.; Charney, J.J.; Potter, B.E.; Goodrick, S.L. The Hot-Dry-Windy Index: A New Fire Weather Index. *Atmosphere* **2018**, *9*, 279.

54. Fromm, M.; Lindsey, D.T.; Servranckx, R.; Yue, G.; Trickl, T.; Sica, R.; Doucet, P.; Godin-Beekmann, S. The Untold Story of Pyrocumulonimbus. *Bulletin of the American Meteorological Society* **2010**, *91*, 1193-1210, doi:10.1175/2010BAMS3004.1.

55. Clements, C.B.; Lareau, N.P.; Seto, D.; Contezac, J.; Davis, B.; Teske, C.; Zajkowski, T.J.; Hudak, A.T.; Bright, B.C.; Dickinson, M.B., et al. Fire weather conditions and fire–atmosphere interactions observed during low-intensity prescribed fires – RxCADRE 2012 %J International Journal of Wildland Fire. **2016**, *25*, 90-101, doi:https://doi.org/10.1071/WF14173.

56. Zhang, X.; Kondragunta, S. Temporal and spatial variability in biomass burned areas across the USA derived from the GOES fire product. *Remote Sensing of Environment* **2008**, *112*, 2886-2897, doi:10.1016/j.rse.2008.02.006.

57. Tan, B.; Dellomo, J.; Folley, C.; Grycewicz, T.; Houchin, S.; Isaacson, P.; Johnson, P.; Porter, B.; Reth, A.; Thiyanaratnam, P., et al. GOES-R series image navigation and registration performance assessment tool set. **2020**, https://doi.org/10.1117/1.JRS.14.032405.

58. Yamamoto, Y.; Ichii, K.; Higuchi, A.; Takenaka, H. Geolocation Accuracy Assessment of Himawari-8/AHI Imagery for Application to Terrestrial Monitoring. *Remote Sens.* **2020**, *12*, 1372.

59. Wang, W.; Li, S.; Hashimoto, H.; Takenaka, H.; Higuchi, A.; Kalluri, S.; Nemani, R. An Introduction to the Geostationary-NASA Earth Exchange (GeoNEX) Products: 1. Top-of-Atmosphere Reflectance and Brightness Temperature. *Remote Sens.* **2020**, *12*, 1267.

60. Bhushan, S.; Barros, A.P. A Numerical Study to Investigate the Relationship between Moisture Convergence Patterns and Orography in Central Mexico. *Journal of Hydrometeorology* **2007**, *8*, 1264-1284, doi:10.1175/2007JHM791.1.

61. Nair, U.S.; Asefi, S.; Welch, R.M.; Ray, D.K.; Lawton, R.O.; Manoharan, V.S.; Mulligan, M.; Sever, T.L.; Irwin, D.; Pounds, J.A. Biogeography of Tropical Montane Cloud Forests. Part II: Mapping of Orographic Cloud Immersion. *Journal of Applied Meteorology and Climatology* **2008**, *47*, 2183-2197, doi:10.1175/2007JAMC1819.1.

62. Nieman, S.J., W. P. Menzel, C. M. Hayden, D. Gray, S. T. Wanzong, C. S., Velden, and J. Daniels, **1997**: Fully automated cloud-drift winds in NESDIS operations. Bull. Amer. Meteor. Soc., 78, 1121–1133, doi:10.1175/1520-0477(1997)078,1121: FACDWI.2.0.CO;2.

63. Bormann, N.; Thépaut, J.-N. Impact of MODIS Polar Winds in ECMWF's 4DVAR Data Assimilation System. *Monthly Weather Review* **2004**, *132*, 929-940, doi:10.1175/1520-0493(2004)132<0929:IOMPWI>2.0.CO;2.

64. Bedka, K.M., Velden, C.S., Petersen, R.A., Feltz, W.F., Mecikalski, J.R. Comparisons of Satellite-Derived Atmospheric Motion Vectors, Rawinsondes, and NOAA Wind Profiler Observations. Journal of Applied Meteorology and Climatology **2009**, 48, 1542-1561, doi:10.1175/2009JAMC1867.1.

65. Cordoba, M., Dance, S.L., Kelly, G.A., Nichols, N.K., Waller, J.A. Diagnosing atmospheric motion vector observation errors for an operational high-resolution data assimilation system. **2017**, *143*, 333-341, doi:10.1002/qj.2925.

66. Jung, J., Marshall, J. Le, Daniels, J., and Riishojgaard, L. P., Investigating height assignment type errors in the NCEP global forecasting system, *Proc. 10th Int. Wind Workshop* **2010**, Tokyo, Japan, Int. Working Winds Group, Session 3: Paper 4., http://www.eumetsat.int/website/home/News/ConferencesandEvents/PreviousEvents/DAT_2042632.html (last accessed 25 September 2020).

67. Salonen, K., J. Cotton, N. Bormann, and M. Forsythe, 2015: Characterizing AMV Height-Assignment Error by Comparing Best-Fit Pressure Statistics from the Met Office and ECMWF Data Assimilation Systems. *J. Appl. Meteor. Climatol.*, **54,** 225–242, DOI: 10.1175/JAMC-D-14-0025.1

68. Velden, C.S., Bedka, K.M. Identifying the Uncertainty in Determining Satellite-Derived Atmospheric Motion Vector Height Attribution. *Journal of Applied Meteorology and Climatology* **2009**, *48*, 450-463, doi:10.1175/2008JAMC1957.1.

69. Forsythe M., Saunders R., AMV errors: A new approach in NWP. In Proceedings of the 9th EUMETSAT International Winds Workshop, 14–18 April 2008. Darmstadt, Germany,

1334   https://www.semanticscholar.org/paper/AMV-errors%3A-a-new-approach-in-NWP-Forsythe-
1335   Saunders/d17415a68fbdddcc6b6c46b2ee779ce8beb3712c?p2df (last accessed 25 September 2020).
1336   70.   Weissmann, M., Folger, K., Lange, H. Height Correction of Atmospheric Motion Vectors Using Airborne
1337   Lidar Observations. *Journal of Applied Meteorology and Climatology* **2013**, *52*, 1868-1877, doi:10.1175/JAMC-
1338   D-12-0233.1.
1339   71.   Hernandez-Carrascal, A., Bormann, N. Atmospheric Motion Vectors from Model Simulations. Part II:
1340   Interpretation as Spatial and Vertical Averages of Wind and Role of Clouds. *Journal of Applied Meteorology
1341   and Climatology* **2014**, *53*, 65-82, doi:10.1175/JAMC-D-12-0337.1.
1342